

Measurement of $\eta\eta$ production in two-photon collisions

S. Uehara,⁸ Y. Watanabe,¹⁴ H. Nakazawa,²⁶ I. Adachi,⁸ H. Aihara,⁴⁴ K. Arinstein,^{1,33} T. Aushev,^{19,12} A. M. Bakich,³⁸ V. Balagura,¹² E. Barberio,²³ A. Bay,¹⁹ K. Belous,¹¹ M. Bischofberger,²⁵ A. Bondar,^{1,33} G. Bonvicini,⁴⁸ A. Bozek,²⁹ M. Bračko,^{21,13} T. E. Browder,⁷ P. Chang,²⁸ Y. Chao,²⁸ A. Chen,²⁶ P. Chen,²⁸ B. G. Cheon,⁶ I.-S. Cho,⁴⁹ Y. Choi,³⁷ J. Dalseno,^{22,40} Z. Doležal,² A. Drutskoy,⁴ S. Eidelman,^{1,33} P. Goldenzweig,⁴ H. Ha,¹⁷ J. Haba,⁸ K. Hayasaka,²⁴ H. Hayashii,²⁵ Y. Horii,⁴³ Y. Hoshi,⁴² W.-S. Hou,²⁸ Y. B. Hsiung,²⁸ H. J. Hyun,¹⁸ R. Itoh,⁸ M. Iwabuchi,⁴⁹ M. Iwasaki,⁴⁴ Y. Iwasaki,⁸ T. Julius,²³ D. H. Kah,¹⁸ J. H. Kang,⁴⁹ P. Kapusta,²⁹ H. Kawai,³ T. Kawasaki,³¹ H. Kichimi,⁸ H. J. Kim,¹⁸ H. O. Kim,¹⁸ J. H. Kim,¹⁶ M. J. Kim,¹⁸ B. R. Ko,¹⁷ P. Kodyš,² S. Korpar,^{21,13} P. Križan,^{20,13} P. Krokovny,⁸ Y.-J. Kwon,⁴⁹ S.-H. Kyeong,⁴⁹ J. S. Lange,⁵ M. J. Lee,³⁶ S.-H. Lee,¹⁷ Y. Liu,²⁸ D. Liventsev,¹² R. Louvot,¹⁹ A. Matyja,²⁹ S. McOnie,³⁸ K. Miyabayashi,²⁵ H. Miyata,³¹ Y. Miyazaki,²⁴ R. Mizuk,¹² G. B. Mohanty,³⁹ T. Mori,²⁴ E. Nakano,³⁴ M. Nakao,⁸ Z. Natkaniec,²⁹ S. Nishida,⁸ K. Nishimura,⁷ O. Nitoh,⁴⁶ S. Ogawa,⁴¹ T. Ohshima,²⁴ S. Okuno,¹⁴ S. L. Olsen,^{36,7} C. W. Park,³⁷ H. Park,¹⁸ H. K. Park,¹⁸ R. Pestotnik,¹³ M. Petrič,¹³ L. E. Piilonen,⁴⁷ A. Poluektov,^{1,33} S. Ryu,³⁶ H. Sahoo,⁷ Y. Sakai,⁸ O. Schneider,¹⁹ C. Schwanda,¹⁰ K. Senyo,²⁴ M. E. Sevier,²³ M. Shapkin,¹¹ C. P. Shen,⁷ J.-G. Shiu,²⁸ B. Shwartz,^{1,33} F. Simon,^{22,40} P. Smerkol,¹³ A. Sokolov,¹¹ E. Solovieva,¹² S. Stanič,³² M. Starič,¹³ T. Sumiyoshi,⁴⁵ Y. Teramoto,³⁴ T. Uglov,¹² Y. Unno,⁶ S. Uno,⁸ G. Varner,⁷ K. Vervink,¹⁹ C. H. Wang,²⁷ P. Wang,⁹ X. L. Wang,⁹ R. Wedd,²³ E. Won,¹⁷ Y. Yamashita,³⁰ Z. P. Zhang,³⁵ V. Zhilich,^{1,33} P. Zhou,⁴⁸ T. Zivko,¹³ and A. Zupanc¹⁵

(Belle Collaboration)

¹*Budker Institute of Nuclear Physics, Novosibirsk*²*Faculty of Mathematics and Physics, Charles University, Prague*³*Chiba University, Chiba*⁴*University of Cincinnati, Cincinnati, Ohio 45221*⁵*Justus-Liebig-Universität Gießen, Gießen*⁶*Hanyang University, Seoul*⁷*University of Hawaii, Honolulu, Hawaii 96822*⁸*High Energy Accelerator Research Organization (KEK), Tsukuba*⁹*Institute of High Energy Physics, Chinese Academy of Sciences, Beijing*¹⁰*Institute of High Energy Physics, Vienna*¹¹*Institute of High Energy Physics, Protvino*¹²*Institute for Theoretical and Experimental Physics, Moscow*¹³*J. Stefan Institute, Ljubljana*¹⁴*Kanagawa University, Yokohama*¹⁵*Institut für Experimentelle Kernphysik, Karlsruher Institut für Technologie, Karlsruhe*¹⁶*Korea Institute of Science and Technology Information, Daejeon*¹⁷*Korea University, Seoul*¹⁸*Kyungpook National University, Taegu*¹⁹*École Polytechnique Fédérale de Lausanne (EPFL), Lausanne*²⁰*Faculty of Mathematics and Physics, University of Ljubljana, Ljubljana*²¹*University of Maribor, Maribor*²²*Max-Planck-Institut für Physik, München*²³*University of Melbourne, School of Physics, Victoria 3010*²⁴*Nagoya University, Nagoya*²⁵*Nara Women's University, Nara*²⁶*National Central University, Chung-li*²⁷*National United University, Miao Li*²⁸*Department of Physics, National Taiwan University, Taipei*²⁹*H. Niewodniczanski Institute of Nuclear Physics, Krakow*³⁰*Nippon Dental University, Niigata*³¹*Niigata University, Niigata*³²*University of Nova Gorica, Nova Gorica*³³*Novosibirsk State University, Novosibirsk*³⁴*Osaka City University, Osaka*³⁵*University of Science and Technology of China, Hefei*³⁶*Seoul National University, Seoul*³⁷*Sungkyunkwan University, Suwon*

³⁸*School of Physics, University of Sydney, NSW 2006*³⁹*Tata Institute of Fundamental Research, Mumbai*⁴⁰*Excellence Cluster Universe, Technische Universität München, Garching*⁴¹*Toho University, Funabashi*⁴²*Tohoku Gakuin University, Tagajo*⁴³*Tohoku University, Sendai*⁴⁴*Department of Physics, University of Tokyo, Tokyo*⁴⁵*Tokyo Metropolitan University, Tokyo*⁴⁶*Tokyo University of Agriculture and Technology, Tokyo*⁴⁷*IPNAS, Virginia Polytechnic Institute and State University, Blacksburg, Virginia 24061*⁴⁸*Wayne State University, Detroit, Michigan 48202*⁴⁹*Yonsei University, Seoul*

(Received 21 July 2010; published 30 December 2010)

We report the first measurement of the differential cross section for the process $\gamma\gamma \rightarrow \eta\eta$ in the kinematic range above the $\eta\eta$ threshold, $1.096 \text{ GeV} < W < 3.8 \text{ GeV}$ over nearly the entire solid angle range, $|\cos\theta^*| \leq 0.9$ or ≤ 1.0 depending on W , where W and θ^* are the energy and η scattering angle, respectively, in the $\gamma\gamma$ center-of-mass system. The results are based on a 393 fb^{-1} data sample collected with the Belle detector at the KEKB e^+e^- collider. In the W range $1.1\text{--}2.0 \text{ GeV}/c^2$ we perform an analysis of resonance amplitudes for various partial waves, and at higher energy we compare the energy and the angular dependences of the cross section with predictions of theoretical models and extract contributions of the χ_{cJ} charmonia.

DOI: [10.1103/PhysRevD.82.114031](https://doi.org/10.1103/PhysRevD.82.114031)

PACS numbers: 13.66.Bc, 13.60.Le, 14.40.Be, 14.40.Pq

I. INTRODUCTION

Measurements of exclusive hadronic final states in two-photon collisions provide valuable information concerning the physics of light- and heavy-quark resonances, perturbative and nonperturbative QCD, and hadron-production mechanisms. So far, we, the Belle Collaboration, have measured the production cross sections for charged-pion pairs [1–3], charged and neutral-kaon pairs [3–5], and proton-antiproton pairs [6]. We have also analyzed D -meson-pair production and observed a new charmonium state identified as the $\chi_{c2}(2P)$ [7]. Recently, we have examined $\omega J/\psi$ and $\phi J/\psi$ production and also found charmoniumlike structures in these final states [8,9].

In addition, we have measured the production cross section for the $\pi^0\pi^0$ and $\eta\pi^0$ final states [10–12]. The statistics of these measurements are 2–3 orders of magnitude higher than in pre- B -factory measurements [13], opening a new era in studies of two-photon physics.

In the present study, we report measurements of the differential cross sections, $d\sigma/d|\cos\theta^*|$, for the process $\gamma\gamma \rightarrow \eta\eta$ in a wide two-photon center-of-mass (c.m.) energy (W) range from the $\eta\eta$ mass threshold 1.096 to 3.8 GeV , and in the c.m. angular range, $|\cos\theta^*| \leq 1$ (0.9) for $W \leq 2.0 \text{ GeV}$ ($W > 2.0 \text{ GeV}$). In this analysis, we use the $\eta \rightarrow \gamma\gamma$ decay mode only because the $\eta \rightarrow \pi^+\pi^-\pi^0$ decay mode has a much smaller product of efficiency and branching fraction.

The $I^G J^{PC}$ quantum numbers of a meson produced by two photons and decaying into $\eta\eta$ are restricted to be $0^+(\text{even})^{++}$, that is, those of $f_{J=\text{even}}$ or $\chi_{cJ=\text{even}}$ mesons. A long-standing puzzle in QCD is the existence and struc-

ture of low mass scalar mesons. In the $I = 0$ sector, we recently observed a peaking structure at the $f_0(980)$ mass in both the $\gamma\gamma \rightarrow \pi^+\pi^-$ and $\gamma\gamma \rightarrow \pi^0\pi^0$ channels [1,10]. Our analysis also suggests the existence of another f_0 meson in the $1.2\text{--}1.5 \text{ GeV}$ region that couples to two photons [10]. The significant $s\bar{s}$ component in the η meson implies a connection of this reaction to the K^+K^- [4] and $K^0\bar{K}^0$ [5] processes.

At higher energies ($W > 2.4 \text{ GeV}$), we can invoke a quark model. In leading-order calculations, the ratio of the $\eta\pi^0$ or $\eta\eta$ cross section to that of $\pi^0\pi^0$ is predicted. Analyses of energy and angular distributions of these cross sections are essential to determine properties of the observed resonances and to test the validity of QCD-based models [14–16] involving $q\bar{q}$ production and SU(3) flavor symmetry. It is also interesting to compare the behavior of $\eta\eta$ production with that of K^+K^- and $K_S^0K_S^0$, which have been measured by the Belle experiment [3,5]. The cross section for the $\gamma\gamma \rightarrow \eta\eta$ process has not been measured so far.

The organization of this paper is as follows. In Sec. II, the experimental apparatus and event selection are described. Signal yields and backgrounds are discussed in Sec. III. Differential cross sections are then extracted in Sec. IV. In Sec. V, the $f_2(1270)$, $f_2'(1525)$, and other possible resonances are studied by parameterizing partial wave amplitudes. The behavior of differential cross sections and W dependence of the integrated cross sections at higher energy region ($W > 2.4 \text{ GeV}$) are compared to QCD predictions in Sec. VI. Finally in Sec. VII, a summary and conclusion are given.

II. EXPERIMENTAL APPARATUS AND EVENT SELECTION

Events with all-neutral final states are extracted from the data collected by the Belle experiment. In this section, the Belle detector and event selection procedure are described.

A. Experimental apparatus

A comprehensive description of the Belle detector is given elsewhere [17]. We mention here only those detector components that are essential for the present measurement. Charged tracks are reconstructed from hit information in the silicon vertex detector and the central drift chamber located in a uniform 1.5 T solenoidal magnetic field. The detector solenoid is oriented along the z axis, which points in the direction opposite to that of the positron beam. Photon detection and energy measurements are performed with a CsI(Tl) electromagnetic calorimeter (ECL).

For this all-neutral final state, we require that there be no reconstructed tracks coming from the vicinity of the nominal collision point. Therefore, the central drift chamber is used to veto events with charged track(s). The photons from a decay of the η meson are detected and their momentum vectors are measured by the ECL. The ECL is also used to trigger signal events. Two kinds of ECL triggers are used to select events of interest: The total ECL energy deposit in the acceptance region used by the trigger (see the next subsection) is greater than 1.15 GeV (the ‘‘HiE’’ trigger), or four or more ECL clusters above an energy threshold of 110 MeV in segments of the ECL (the ‘‘Clst4’’ trigger). The above energy thresholds are determined by studying the correlations between the two triggers in the experimental data.

B. Experimental data and data filtering

We use a 393 fb^{-1} data sample accumulated by the Belle detector at the KEKB asymmetric-energy e^+e^- collider [18]. For an early part of Belle data taking, all-neutral final states were not recorded. Thus, this data set is smaller than the hadronic data sample available at Belle.

The data were recorded at several e^+e^- c.m. energy regions summarized in Table I. We combine the results from the different beam energies, because the e^+e^- c.m.

TABLE I. Data sample: integrated luminosities and energies.

e^+e^- c.m. energy (GeV)	Integrated luminosity (fb^{-1})	Runs
10.58	286	Y(4S)
10.52	33	Continuum
9.43–9.46	7.3	Near Y(1S)
9.99–10.03	6.7	Near Y(2S)
10.32–10.36	3.2	Near Y(3S)
10.83–11.02	58	Near Y(5S)
Total	393	

energy is more than twice our $\gamma\gamma$ c.m. energy range for any of the beam energies, and the beam-energy dependence of the two-photon luminosity function is rather small. We generate most of the signal Monte Carlo (MC) events and calculate the two-photon luminosity function for 10.58 GeV. We then derive a correction factor for the other beam energies. The correction is less than 0.5% over the full range of $\gamma\gamma$ c.m. energies considered here. The signal MC and the beam-energy dependences are described in Sec. IV C.

The analysis is carried out in the ‘‘zero-tag’’ mode, where neither the recoil electron nor positron are detected. We restrict the virtuality of the incident photons to be small by imposing a strict requirement on the transverse-momentum balance with respect to the beam axis for the final-state hadronic system.

The filtering procedure (‘‘neutral skim’’) used for this analysis is the same as the one used for $\pi^0\pi^0$ and $\eta\pi^0$ studies [10–12]. The important requirements in this filter are the following: There are no tracks originating in the beam collision region and having a transverse momentum greater than 0.1 GeV/ c in the laboratory frame; two or more photons that satisfy a specified energy or transverse-momentum criterion; this requirement is satisfied when there are three or more photons each with an energy above 100 MeV. The performance of the ECL triggers is studied in detail using $\pi^0\pi^0$ events [10]. We also study the trigger thresholds using the $\eta\eta$ signal samples.

C. Event selection

From the neutral skim event sample, we select $\gamma\gamma \rightarrow \eta\eta$ candidates that satisfy the following conditions:

- (1) The total energy deposit in ECL is less than 5.7 GeV;
- (2) each photon candidate is required to have an energy of at least 100 MeV, and events with four such photons are selected;
- (3) the event is triggered by either the ECL trigger HiE or Clst4;
- (4) either the sum of the energies of the photons in the acceptance region used by the trigger is larger than 1.25 GeV, or all four selected photons are within this region, where the trigger acceptance is the polar-angle range $-0.6255 < \cos\theta < +0.9563$ in the laboratory frame;
- (5) of the three possible combinations that can be constructed from the four photons, there is one in which each invariant mass of the two-photon pairs satisfies $0.52 \text{ GeV}/c^2 < M_{\gamma\gamma i} < 0.57 \text{ GeV}/c^2$, where $i = 1, 2$ is an index of the two-photon pairs;
- (6) there is no neutral pion combination that is constructed from any two of the four photons with a χ^2 smaller than 9 in the mass-constrained fit;
- (7) the transverse momentum for the $\eta\eta$ system $|\Sigma \mathbf{p}_i^*|$ is required to be less than 0.05 GeV/ c .

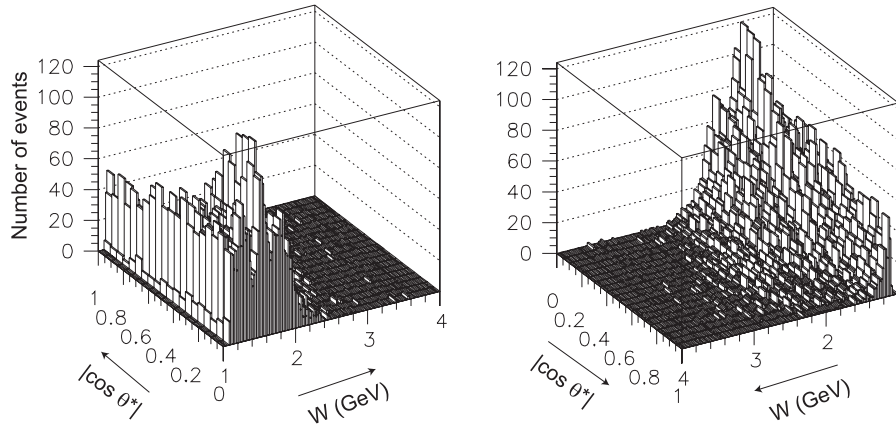


FIG. 1. Two-dimensional W and $|\cos\theta^*|$ distribution for the $\eta\eta$ candidates in data. The same distribution is viewed from two different directions. The backgrounds are not subtracted.

A small fraction of events contain multiple combinations of the four photons that satisfy criterion (5). In those events, we take only one combination whose residual for the nominal η mass ($m_\eta = 0.5478 \text{ GeV}/c^2$), $(M_{\gamma\gamma_1} - m_\eta)^2 + (M_{\gamma\gamma_2} - m_\eta)^2$, is the smallest.

We then scale the energy of the two photons with a factor that is the ratio of the nominal η mass to the reconstructed mass: $m_\eta/M_{\gamma\gamma_i}$. This is equivalent to an approximate 1C (one constraint) mass constraint fit in which the relative energy resolution ($\Delta E/E$) is independent of E and the resolution in the angle measurement is much better than that of the energy. This is a good approximation for the η 's in this momentum range. Using the corrected four-momenta of the η mesons, we calculate the invariant mass (W) and the transverse momentum ($|\Sigma \mathbf{p}_t^*|$) in the e^+e^- c.m. frame for the $\eta\eta$ system and apply cut (7) above. We select 31 655 candidates in the region $W < 4.0 \text{ GeV}$.

We define the c.m. scattering angle θ^* as the scattering angle of the η . The e^+e^- direction is used to approximate the axis for the polar-angle calculation because the exact $\gamma\gamma$ axis is unknown for untagged events. The two-dimensional ($W, |\cos\theta^*|$) distribution of selected events is shown in Fig. 1.

The probability for a signal $\eta\eta$ event to have multiple combinations is sizable only near the threshold (about 6% at $W \sim 1.11 \text{ GeV}$), but it is small (less than 2%) above $W > 1.12 \text{ GeV}$, according to the signal MC samples. For different choices of γ -pair combinations in an event, the W values are nearly the same, but $|\cos\theta^*|$ can be different. As the angular distribution is observed to be flat near the threshold, which is also theoretically expected, the effect of an incorrect choice is negligibly small.

III. YIELDS OF THE SIGNAL AND BACKGROUNDS

In this section, backgrounds are identified and subtracted and the extraction of the signal yield is discussed.

A. Determination of non- $\eta\eta$ background

There are two kinds of background processes for the $\gamma\gamma \rightarrow \eta\eta$ signal process: non- $\eta\eta$ and $\eta\eta X$ backgrounds. The non- $\eta\eta$ background does not contain an η pair in the final state, while the $\eta\eta X$ background includes extra particle(s) in the final state in addition to the $\eta\eta$ combination. In this measurement, the non- $\eta\eta$ contribution, arising from beam backgrounds or other physics processes, is the dominant background in the final sample.

We first determine the number of the non- $\eta\eta$ background events using the yields of $\eta\eta$ mass sidebands. After subtracting this background contribution, we check the p_t -balance distribution for the remaining component; the signal component peaks near $|\Sigma \mathbf{p}_t^*| = 0$, while we expect that the $\eta\eta X$ background does not.

1. Defining the $\eta\eta$ -mass sidebands

The $\eta\eta$ -mass sidebands are defined by displacing the central points of the mass intervals in selection criterion (5) by $\pm 0.07 \text{ GeV}/c^2$. Two kinds of sidebands are defined: sideband A and sideband B. In sideband A, the central points for the two-dimensional mass cut for $(M_{\gamma\gamma_1}, M_{\gamma\gamma_2})$ are (here, we assume $M_{\gamma\gamma_1} < M_{\gamma\gamma_2}$) (0.545, 0.615) and (0.475, 0.545) in units of GeV/c^2 , and the width of the range is $\pm 0.025 \text{ GeV}/c^2$. Sideband B has central points (0.475, 0.475), (0.475, 0.615), and (0.615, 0.615). When there are two or more choices of γ -pair combinations in an event that fall in the same sideband box, we take the one that is closest to the nominal central point of each sideband box: $(m_\eta - 0.07, m_\eta)$ or $(m_\eta, m_\eta + 0.07)$ for sideband A and $(m_\eta \pm 0.07, m_\eta \pm 0.07)$ for sideband B. This is similar to the multiple candidate selection applied for the signal candidates. The $M_{\gamma\gamma}$ distributions near the signal and sideband regions are shown in Fig. 2.

We also calculate W and $|\cos\theta^*|$ for the sideband A and B candidates by scaling $M_{\gamma\gamma_i}$ to m_η (not to $m_\eta \pm 0.07$, which would change the threshold mass).

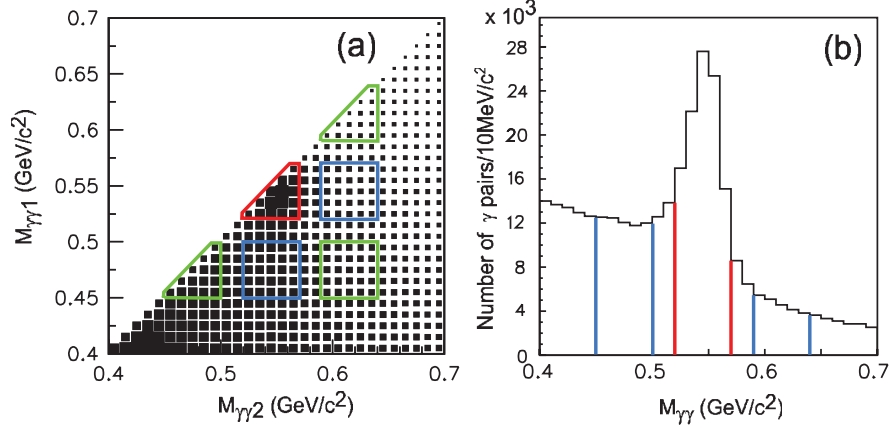


FIG. 2 (color). (a) Two-dimensional $M_{\gamma\gamma 1}$ vs $M_{\gamma\gamma 2}$ distribution of the four-photon candidates in data. We take $M_{\gamma\gamma 1} < M_{\gamma\gamma 2}$. The p_t -balance cut with $p_t < 0.1$ GeV/c is applied using the photon momenta before the m_η mass correction, which reduces backgrounds. Red, blue, and green boxes show the signal, sideband A, and sideband B regions, respectively. (b) A one-dimensional projection of the same distribution where the $\gamma\gamma$ pair on the opposite side is required to be in the signal mass region 0.52–0.57 GeV/c². The vertical red and blue lines show the signal and two sideband A regions, respectively. Note that there are two entries per event in the signal region.

2. Sideband subtraction

We subtract the sideband yield to obtain the signal component with the following formula:

$$Y = Y_s - 0.5Y_{bA} + 0.25Y_{bB},$$

where Y is the signal yield after sideband subtraction, Y_s is the yield in the observed events in the signal region, and Y_{bA} (Y_{bB}) the yield of the sideband A (B) region. Here we model the non- η backgrounds with a linear distribution in $M_{\gamma\gamma}$, for backgrounds with both η non- η and non- η non- η combinations. The possibility of a nonlinear background component is included in the systematic error (see Sec. IV E). The yield in the signal and sideband regions (before the sideband subtraction) is shown in Fig. 3. To obtain the differential cross sections, we subtract bin by bin in each two-dimensional bin of $(W, |\cos\theta^*|)$ with bin widths $\Delta W = 20$ MeV and $\Delta|\cos\theta^*| = 0.1$. Two or five W bins are combined later in the determination of the final cross sections. Signal leakage into the sideband regions, which amounts to 2%–5% of the signal size Y and is larger at small W , is expected according to signal MC simulations. This effect is corrected in the derivation of the differential cross sections by reducing the efficiency.

B. p_t -unbalanced component

We expect that the background remaining after the $\eta\eta$ sideband subtraction is very small. To confirm this, we examine the W dependence of the yield ratio of the p_t -unbalanced component R defined as

$$R = \frac{Y(0.15 \text{ GeV}/c < |\sum \mathbf{p}_t^*| < 0.20 \text{ GeV}/c)}{Y(|\sum \mathbf{p}_t^*| < 0.05 \text{ GeV}/c)}, \quad (1)$$

where Y is the yield after the sideband subtraction in the specified p_t region. R is plotted as a function of W in Fig. 4,

where any excess over the signal MC would indicate a contribution from $\eta\eta X$ background. There is such a small excess just above mass threshold. We include the effect from this possible background source into the correction and the systematic error. Non- $\eta\eta$ background is much larger near the W threshold, and this excess may be due to an imperfect sideband subtraction. We apply a -3% correction for the background from this source for

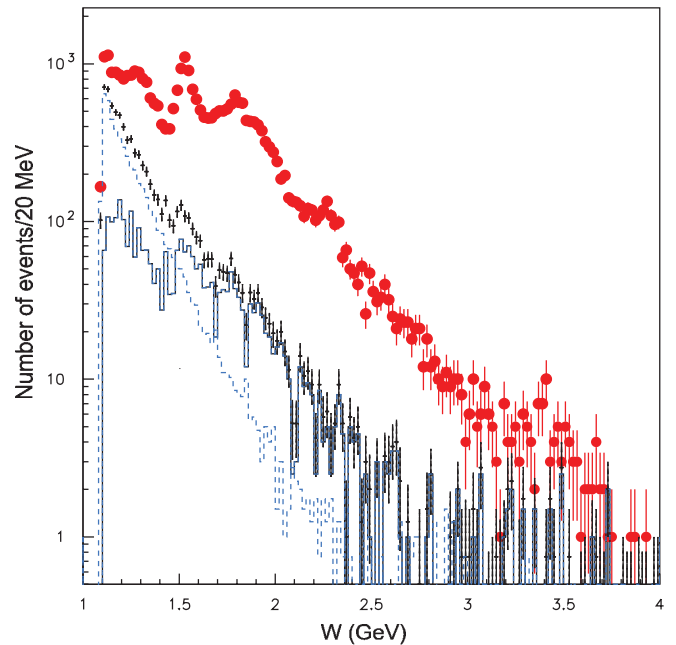


FIG. 3 (color). W distributions of the yields in the signal region (closed circles with error bars, Y_s) and estimates of backgrounds of the η non- η component [solid histogram, $0.5(Y_{bA} - Y_{bB})$] and the non- η non- η component (dashed histogram, $0.25Y_{bB}$). Points with error bars show the estimated total background $0.5Y_{bA} - 0.25Y_{bB}$.

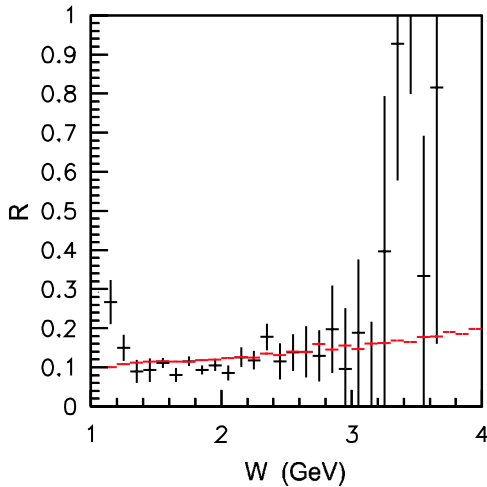


FIG. 4 (color online). Energy dependence of R defined in Eq. (1). It indicates the level of $\eta\eta X$ background contamination, for the experimental data (after the sideband subtraction, points with error bars) and signal MC (short horizontal bars).

$W < 1.2$ GeV. In the W region between 1.2 and 3.3 GeV, the R value is consistent with the signal MC simulation. The reason why the experimental data seem to be slightly below the MC for R in the 1.4–2.0 GeV range is not known, but the difference translated to the background ratio is negligibly small, less than 1%. For $W > 3.3$ GeV, there could be much larger $\eta\eta X$ backgrounds. As described in Sec. IV C, we do not report cross section results for $W > 3.3$ GeV and apply a -3% correction for 3.2 GeV $< W < 3.3$ GeV.

We conclude that this kind of background is less than 2% throughout the W region 1.2–3.2 GeV and assign 2% as the systematic error for this source for the entire W region 1.096–3.3 GeV. These factors are obtained by assuming a quasilinear $|\sum \mathbf{p}_i^*|$ dependence of the background and extracting its leakage into the signal region ($|\sum \mathbf{p}_i^*| < 0.05$ GeV/ c), which is approximately 1/6 of the yield in the 0.15 GeV/ $c < |\sum \mathbf{p}_i^*| < 0.20$ GeV/ c region.

IV. DERIVING DIFFERENTIAL CROSS SECTIONS

In this section, we present the procedure to derive differential cross sections.

A. Effect of e^+e^- beam energy

We generate standard MC events for an e^+e^- c.m. energy $\sqrt{s} = 10.58$ GeV. We compare the products of the luminosity function and efficiency [$L_{\gamma\gamma}(W)\epsilon$ in Eq. (2)] at three different c.m. energies 9.46 GeV($Y(1S)$), 10.58 GeV($Y(4S)$), and 10.87 GeV($Y(5S)$) using MC samples. We conclude that, taking into account the integrated luminosities of the different c.m. energies, the correction factors for the lower and higher energy samples

cancel almost exactly. Applying the MC results for 10.58 GeV to all samples leads to negligibly small effects of less than 0.5%.

B. Invariant mass resolution

We estimate the invariant mass resolution of the $\eta\eta$ system using the signal MC simulation. Since we apply an energy rescaling using the η mass, the W resolution is better than that for a pure energy measurement. We find that the invariant mass resolution is about 0.6% near the threshold, $W = 1.1$ – 1.5 GeV, and approaches 1.0% for higher W . We confirm that the experimental resolution is at most 10% larger than the MC resolution from measurements of p_t balance in $\pi^0\pi^0$ production and in the η' peak in $\gamma\gamma \rightarrow \eta' \rightarrow \gamma\gamma$. The resolution is much smaller than the W bin widths: $\Delta W = 0.04$ or 0.1 GeV. Since statistics are low, we do not unfold our results as in previous measurements [10–12].

C. Determination of the efficiency

The signal MC simulations for $e^+e^- \rightarrow e^+e^-\eta\eta$ are generated using the TREPS code [19] and are used for the efficiency calculation at 32 fixed W points between 1.1 and 4.0 GeV and isotropically in $|\cos\theta^*|$. We evaluate the efficiencies separately in $|\cos\theta^*|$ bins with a width of 0.05, and thus the angular distribution at the generator level does not play a role in the efficiency determination.

The Q_{\max}^2 parameter that gives a maximum virtuality of the incident photons is set to 1.0 GeV², while the cross sections for virtual photon collisions include a form factor: $\sigma_{\gamma\gamma}(0, Q^2) = \sigma_{\gamma\gamma}(0, 0)/(1 + Q^2/W^2)^2$. Our analysis is not sensitive to the form-factor assumption, since our stringent p_t -balance cut ($|\sum \mathbf{p}_i^*| < 0.05$ GeV/ c) implies Q^2/W^2 is much smaller than unity; an approximate relation $Q^2 \sim |\sum \mathbf{p}_i^*|^2$ holds when only one incident photon is treated as moderately virtual and the scattering angle of an electron (or a positron) that has emitted the virtual photon is small. Using a signal MC simulation and replacing the Q^2/W^2 term by either Q^2/m_ρ^2 or omitting it entirely, we confirm that the effect of the form-factor choice on the cross section is less than 0.5%, where m_ρ is the ρ meson mass.

Samples of 400 000 events are generated at each W point and are passed through the detector and trigger simulations. The obtained efficiencies are fitted to a two-dimensional function of $(W, |\cos\theta^*|)$ with an empirical functional form.

We embed background hit patterns from random trigger data into MC events. We find that different samples of background hits give small variations in the selection efficiency determination. A W -dependent error in the efficiency, 3%–4%, arises from the uncertainty in this effect. Figure 5 shows the two-dimensional dependence of the efficiency on $(W, |\cos\theta^*|)$ after the smoothing fit.

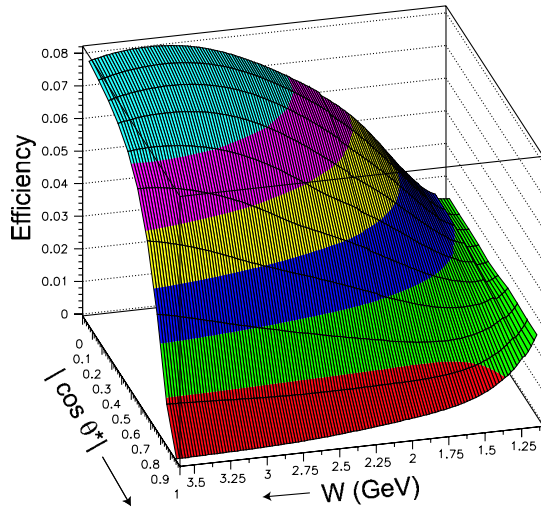


FIG. 5 (color online). Two-dimensional dependence of the efficiency on $(W, |\cos\theta^*|)$.

D. Derivation of differential cross sections

The differential cross section for each $(W, |\cos\theta^*|)$ point is given by

$$\frac{d\sigma}{d|\cos\theta^*|} = \frac{\Delta Y}{\Delta W \Delta |\cos\theta^*| \int \mathcal{L} dt L_{\gamma\gamma}(W) \epsilon \mathcal{B}^2}, \quad (2)$$

where ΔY is the signal yield after the η -mass sideband subtraction, ΔW and $\Delta |\cos\theta^*|$ are the bin widths, $\int \mathcal{L} dt$ and $L_{\gamma\gamma}(W)$ are the integrated luminosity and two-photon luminosity function calculated with TREPS [19], respectively, ϵ is the efficiency, and \mathcal{B}^2 is the squared branching fraction for $\eta \rightarrow \gamma\gamma$. The oversubtraction of signal in the sideband due to the leakage of the signal into the sideband region is evaluated in the MC, separately, and finally included in the efficiency ϵ .

The bin sizes ΔW and $\Delta |\cos\theta^*|$ and the maximum $|\cos\theta^*|$ for which we obtain the differential cross section are summarized in Table II. We first derive the differential cross sections for bin widths of $\Delta W = 0.02$ GeV and $\Delta |\cos\theta^*| = 0.1$ and average the differential cross section over two or five different W regions to obtain results for $\Delta W = 0.04$ or 0.10 GeV, respectively.

We do not give a cross section for $W > 3.3$ GeV. In the W range 3.3–3.6 GeV, the charmonium component dominates the yield, and we cannot subtract it in a model-

TABLE II. Bin sizes. The lowest bound of the first W range (1.0957 GeV) corresponds to the mass threshold.

W range (GeV)	ΔW (GeV)	$\Delta \cos\theta^* $	Maximum $ \cos\theta^* $
1.0957–1.12	0.0243	0.1	1.0
1.12–2.0	0.04	0.1	1.0
2.0–2.4	0.04	0.1	0.9
2.4–3.3	0.10	0.1	0.9

independent way. We also cannot give the cross section including the charmonium contribution in these bins, because leakages from the narrow χ_{c0} peak around 3.41 GeV into adjacent bins due to energy resolution complicate the extraction of cross sections in each bin. Above $W > 3.6$ GeV, we do not find any significant signal after consideration of the backgrounds.

Figure 6 shows the angular dependence of the differential cross sections for selected W bins. Figure 7 shows the cross section integrated over $|\cos\theta^*| < 0.9$ for the entire W range and that for $|\cos\theta^*| < 1.0$ in the range $W < 2.0$ GeV.

E. Systematic errors

Various sources of systematic uncertainties assigned for the $\eta\eta$ signal yield, efficiency, and the cross section evaluation are described in detail below and summarized in Table III.

- (1) *Trigger efficiency.*—The systematic error due to uncertainty in the threshold for the Clst4 trigger (~ 110 MeV) is very small, because photons from η decays have high enough energy. However, the efficiency of the HiE trigger dominates that of Clst4 except in the lowest W region, because the former has a looser condition for the number of clusters in the acceptance region of the trigger. We estimate the uncertainty in the efficiency for the HiE trigger to be 4% over the whole W region and treat it as the combined systematic error for the two kinds of triggers.
- (2) *η selection efficiency.*—We assign 6% for the selection of the two η 's. This corresponds to a 3% uncertainty for the efficiency of each η reconstruction.
- (3) *Overlapping hits from beam background and related effects.*—We assign a 4% (3%) error for $W < 1.44$ GeV ($W > 1.44$ GeV) for uncertainties of the inefficiency in event selection due to beam-background photons, which affect the photon multiplicity and η reconstruction. The uncertainty is estimated by comparing efficiencies among different experimental periods and background conditions. We adopt the average efficiency from different background files, and the uncertainty in the average, obtained from the variation of experimental yield in different run periods, is assigned as the error.
- (4) *p_T -balance cut.*—A 3% uncertainty is assigned. The p_T -balance distribution for the signal is well reproduced by MC so that the efficiency is correct to within this error.
- (5) *Sideband background subtraction.*—1/3 of the size of the subtracted component is assigned to this source for each bin. We conservatively assign this error because we ignore the nonlinear behavior

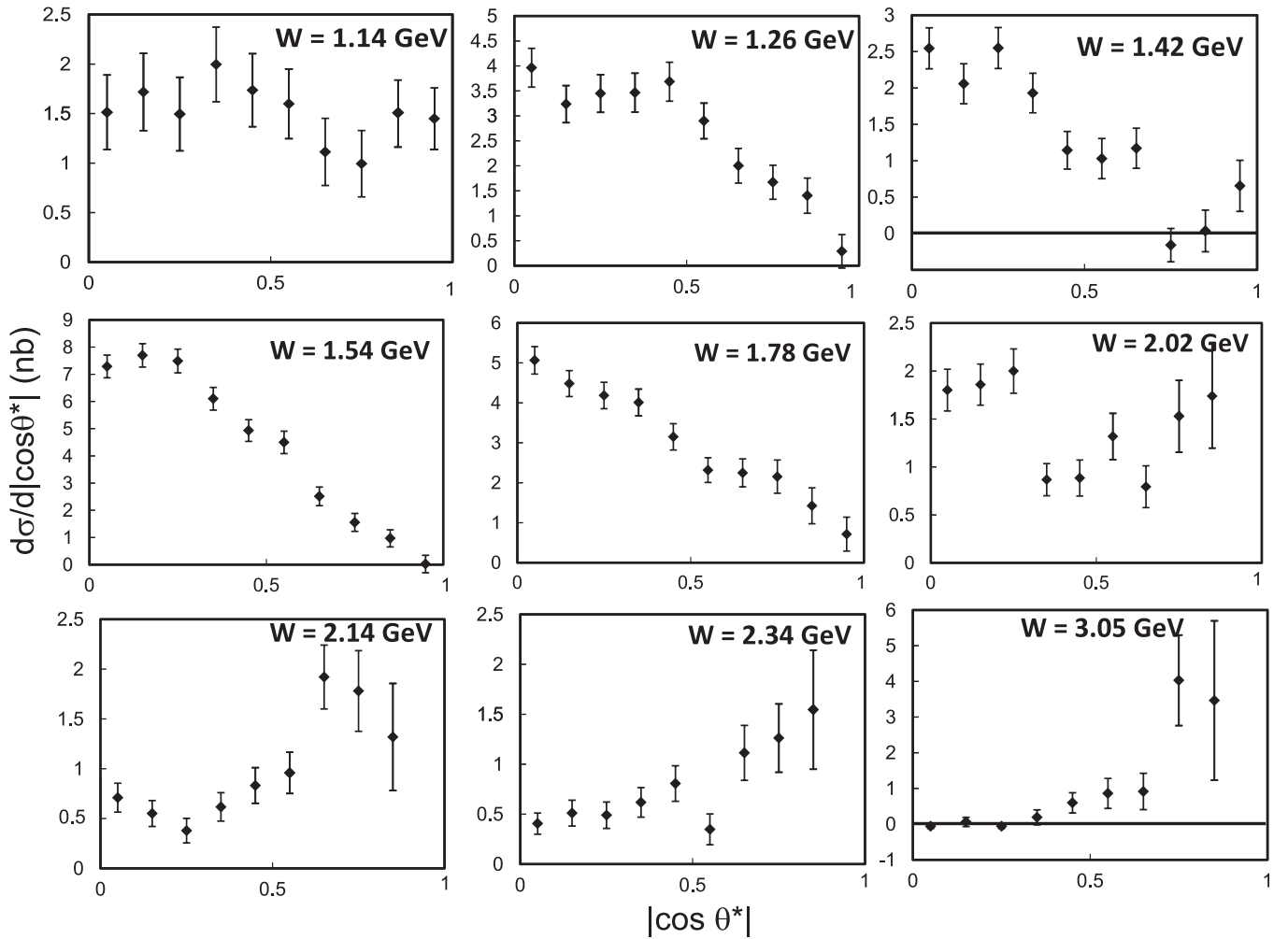


FIG. 6. Angular dependence of the differential cross sections for nine selected W bins indicated. The bin sizes are summarized in Table II.

of the background in the $M_{\gamma\gamma}$ distribution in the sideband subtraction. This effect is expected to be large but cannot be determined precisely in the lowest W bins.

- (6) *p_T -unbalanced background.*—We have applied a -3% correction for this background source only in the lowest and highest W regions, $W < 1.2$ GeV and $W > 3.2$ GeV, respectively. We do not find any evidence of such a component, and no correction is applied for this effect in the other energies. We assign a 2% error from this source for the entire W region.
- (7) *Luminosity function.*—We assign 4% (5%) for W below (above) 3.0 GeV; this includes the uncertainties in the equivalent photon approximation [3% (4%)], the radiative corrections that were neglected (1% – 2%), and the integrated luminosity (1.4%).
- (8) *No unfolding.*—Uncertainty from smearing effects is estimated by smearing a modeled resonance func-

tion with the W resolution and examining apparent changes of the cross section. The changes are large ($\sim 7\%$) only near the slopes of the narrowest resonant structure, in the region 1.44 GeV $\leq W \leq 1.60$ GeV, and smaller (4%) in other W ranges.

- (9) *Other efficiency errors.*—An error of 4% is assigned for uncertainties in the efficiency determination based on MC including the smoothing procedure.

The total systematic error is obtained by adding all the sources in quadrature and is 11% – 12% for the intermediate and high W regions. It becomes more than 20% for $W < 1.24$ GeV.

In the resonance analyses for $W < 2.0$ GeV in Sec. V, we treat the systematic error sources except for (9) as uncertainties in the overall normalization, which are correlated in the different (W , $|\cos\theta^*|$) bins. For the analysis of the W dependence in the high energy region (Sec. VIB), we also take into account energy-dependent deviations for sources (6) and (8).

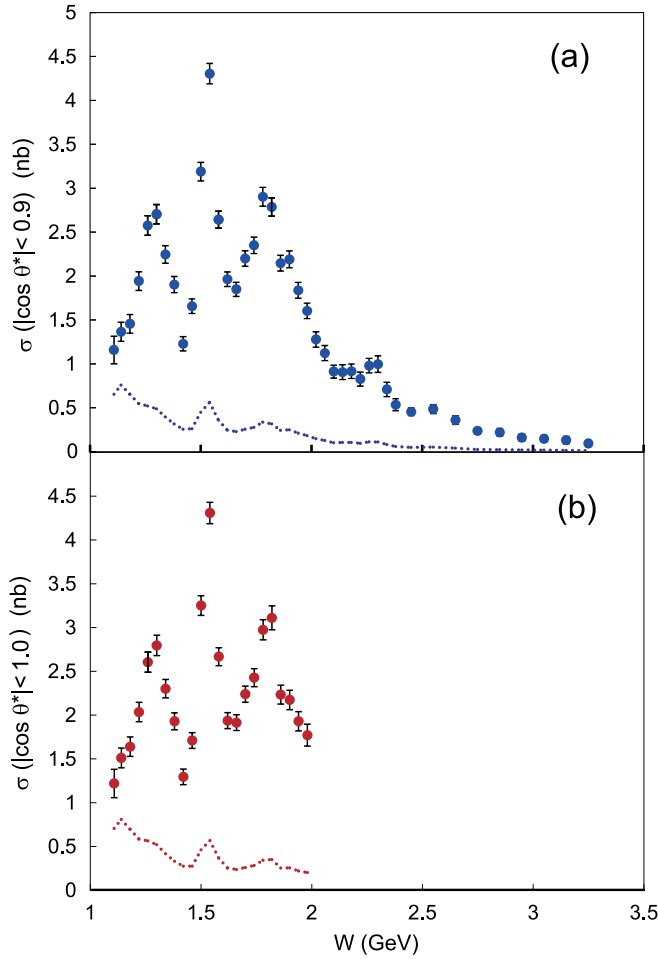


FIG. 7 (color online). The cross section integrated (a) over $|\cos\theta^*| < 0.9$ and (b) over $|\cos\theta^*| < 1.0$ for $W < 2.0$ GeV. Errors are statistical only. The dotted curve shows the size of the systematic uncertainty.

TABLE III. Systematic errors for the differential cross sections. Ranges of errors are shown when they depend on W .

Source	Error (%)
Trigger efficiency	4
η -pair reconstruction efficiency	6
Overlapping hits from beam background, etc.	3–4
p_T -balance cut	3
Sideband background subtraction	2–27 (for $W > 1.2$ GeV) 28–60 (for $W < 1.2$ GeV)
p_T -unbalanced background subtraction	2
Luminosity function and integrated luminosity	4–5
Unfolding	4–7
Other efficiency errors	4
Overall	11–29 (for $W > 1.2$ GeV) 30–61 (for $W < 1.2$ GeV)

V. STUDY OF RESONANCES

In the total cross section (Fig. 7), clear peaks due to the $f_2(1270)$ and $f_2'(1525)$ are visible along with other possible resonances. In this section, we first present consistency checks with previous measurements and report improved measurements of some of these resonances.

A. Differential cross sections in partial waves

In the energy region $W \leq 3$ GeV, $J > 4$ partial waves (next is $J = 6$) may be neglected so that only S, D, and G waves are considered. The differential cross section can be expressed as

$$\frac{d\sigma}{d\Omega}(\gamma\gamma \rightarrow \eta\eta) = |SY_0^0 + D_0Y_2^0 + G_0Y_4^0|^2 + |D_2Y_2^2 + G_2Y_4^2|^2, \quad (3)$$

where D_0 and G_0 (D_2 and G_2) denote the helicity 0 (2) components of the D and G waves, respectively,¹ and Y_J^λ are the spherical harmonics in which the helicity λ is quantized along the $\gamma\gamma$ axis. Since the $|Y_J^\lambda|$'s are not independent of each other, partial waves cannot be separated from the information in the differential cross sections alone.

We rewrite Eq. (3) as

$$\frac{d\sigma}{4\pi d|\cos\theta^*|}(\gamma\gamma \rightarrow \eta\eta) = \hat{S}^2|Y_0^0|^2 + \hat{D}_0^2|Y_2^0|^2 + \hat{D}_2^2|Y_2^2|^2 + \hat{G}_0^2|Y_4^0|^2 + \hat{G}_2^2|Y_4^2|^2. \quad (4)$$

The amplitudes \hat{S}^2 , \hat{D}_0^2 , \hat{D}_2^2 , \hat{G}_0^2 , and \hat{G}_2^2 can be expressed in terms of S , D_0 , D_2 , G_0 , and G_2 [10]. Since the squares of spherical harmonics are independent of each other, we can fit differential cross sections to obtain \hat{S}^2 , \hat{D}_0^2 , \hat{D}_2^2 , \hat{G}_0^2 , and \hat{G}_2^2 in each W bin. Since $|Y_4^0|^2$ and $|Y_4^2|^2$ are nearly equal for $|\cos\theta^*| < 0.7$, we also fit $\hat{G}_0^2 + \hat{G}_2^2$ and $\hat{G}_0^2 - \hat{G}_2^2$. Two types of fits are made: the “SD” fit and “SDG” fit. G waves are neglected in the SD fit.

The spectra of \hat{S}^2 , \hat{D}_0^2 , and \hat{D}_2^2 obtained for the SD fit and \hat{G}_0^2 , \hat{G}_2^2 , and $\hat{G}_0^2 \pm \hat{G}_2^2$ for the SDG fit are shown in Figs. 8 and 9. The spectra of \hat{S}^2 , \hat{D}_0^2 , and \hat{D}_2^2 for the SDG fit are omitted because they are nearly the same as those for the SD fit with somewhat larger statistical errors. It appears that the D_0 and G waves are small enough to be neglected in the region of interest ($W < 2.0$ GeV). In that case, \hat{S}^2 and \hat{D}_2^2 become $|S|^2$ and $|D_2|^2$, respectively, which simplifies the parameterization. In the fits performed here, we neglect the G waves completely and take $D_0 = 0$ in the nominal fit.

¹We denote individual partial waves by roman letters and parameterized waves by italic.

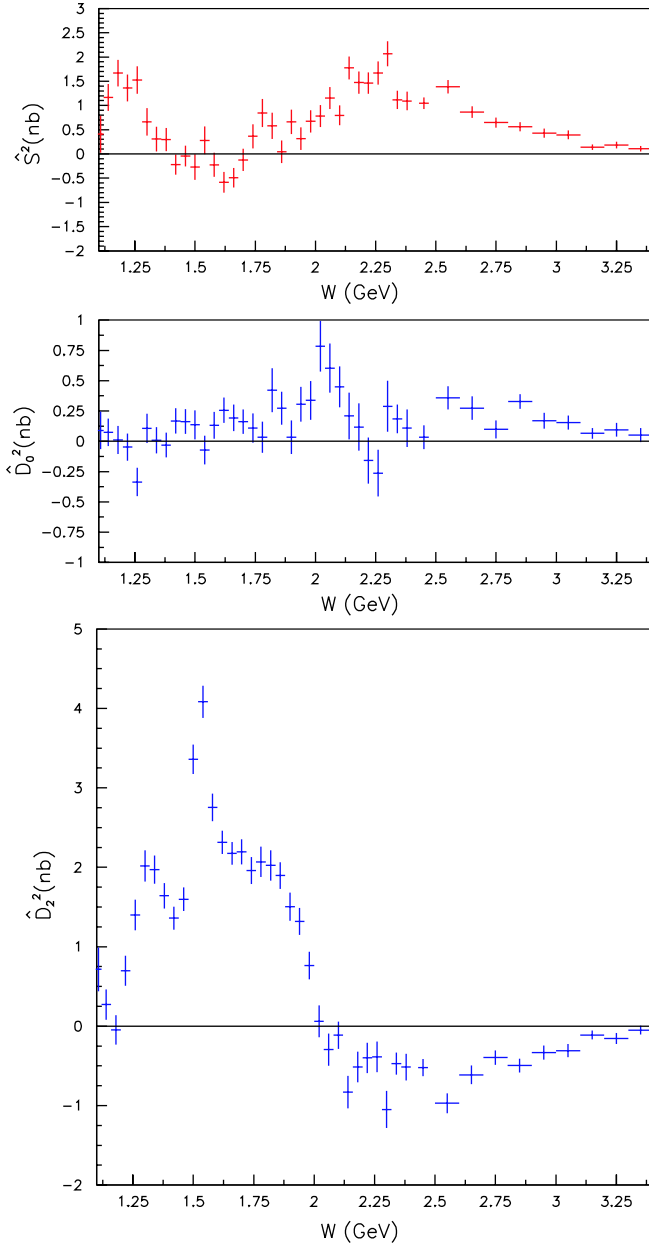


FIG. 8 (color online). Spectra of \hat{S}^2 , \hat{D}_0^2 , and \hat{D}_2^2 for the SD fit. Those for the SDG fit are nearly identical with larger statistical errors. The error bars shown are statistical errors that do not include correlations.

B. Fitting partial wave amplitudes

In this subsection, we describe the extraction of resonant substructure by fitting differential cross sections by parameterizing partial wave amplitudes in terms of resonances and smooth “backgrounds.” Note that we do not fit \hat{S}^2 , \hat{D}_0^2 , and \hat{D}_2^2 but instead fit the differential cross sections directly. Once the functional forms of amplitudes are assumed, we can use Eq. (3) to fit differential cross sections. We then do not have to worry about the correlations between \hat{S}^2 , \hat{D}_0^2 , and \hat{D}_2^2 . The \hat{S}^2 , \hat{D}_0^2 , and \hat{D}_2^2 spectra

are compared with the results of parameterization. Here we neglect the D_0 and G waves in the fitting region $W < 2.00$ GeV.

Quite a few resonances are listed in Ref. [20] (PDG) that are known to decay into $\eta\eta$ with measured or unknown branching fractions to two photons. Besides the $f_2(1270)$ and $f_2'(1525)$, there are $f_2(1565)$, $f_2(1910)$, and $f_2(1950)$ tensor mesons, $f_0(1370)$, $f_0(1500)$, $f_0(1710)$, and $f_0(2020)$ scalar mesons, and spin-4 $f_4(2050)$ states. So far quantitative measurements of the branching fraction to $\eta\eta$ based on observed enhancements in mass spectra are available for $f_2(1270)$ [21,22] and $f_2'(1525)$ [23]. In addition, a phenomenological derivation of the $\eta\eta$ branching fraction based on a K -matrix approach [24] has been tried for $f_2'(1525)$ [20].

To investigate this complicated region, we divide our analysis into two parts. First, we try to confirm or improve the parameter $\Gamma_{\gamma\gamma}\mathcal{B}(\eta\eta)$ of the well established tensor mesons $f_2(1270)$ and $f_2'(1525)$ by fitting in the region $W < 1.64$ GeV. We then investigate the higher mass region by fixing most of the parameters in the fit from results in the low mass region.

1. Low mass region, 1.12–1.64 GeV

We concentrate on the resonances $f_2(1270)$ and $f_2'(1525)$ by fitting the region $W < 1.64$ GeV. The resonances taken into account are $f_2(1270)$, $f_2'(1525)$, and “ $f_0(Y)$,” where $f_0(Y)$ is just a parameterization motivated by $f_0(1370)$ and $f_0(1500)$. We parameterize partial waves as follows:

$$\begin{aligned} S &= A_{f_0(Y)}e^{i\phi_Y} + B_S e^{i\phi_s}, & D_0 &= B_{D_0}, \\ D_2 &= A_{f_2(1270)}e^{i\phi_2} + A_{f_2'(1525)}e^{i\phi_5} + B_{D_2}, \end{aligned} \quad (5)$$

where $A_{f_0(Y)}$, $A_{f_2(1270)}$, and $A_{f_2'(1525)}$ are the amplitudes of the corresponding resonances; B_S , B_{D_0} , and B_{D_2} are “background” amplitudes for S , D_0 , and D_2 waves; ϕ_Y , ϕ_2 , and ϕ_5 are the phases of resonances relative to background amplitudes; and ϕ_s is the relative phase between S and D_0 . We set $B_{D_0} = 0$ (and then $\phi_s = 0$) for simplicity in the nominal fit, but we later consider a nonzero D_0 contribution to determine the systematic errors for the obtained resonance parameters and leave the B_{D_0} symbol here.

To parameterize resonances, we use a relativistic Breit-Wigner amplitude $A_R(W)$ for each spin- J resonance R of mass m_R given by

$$A_R^J(W) = \sqrt{\frac{8\pi(2J+1)m_R}{W}} \frac{\sqrt{\Gamma_{\text{tot}}(W)\Gamma_{\gamma\gamma}(W)\mathcal{B}(R \rightarrow \eta\eta)}}{m_R^2 - W^2 - im_R\Gamma_{\text{tot}}(W)}. \quad (6)$$

For scalar mesons, partial and total widths do not depend on W , while for tensor mesons [$f_2(1270)$,

TABLE IV. Parameters of $f_2(1270)$ and $f_2'(1525)$ assumed or fitted in Ref. [2].

Parameter	$f_2(1270)$	$f_2'(1525)$	Unit	Reference
Mass	1275.1 ± 1.2	1525 ± 5	MeV/ c^2	[20]
Width	$185.1^{+2.9}_{-2.4}$	73^{+6}_{-5}	MeV	[20]
$\mathcal{B}(f_2 \rightarrow \pi\pi)$	$(84.8^{+2.4}_{-1.2})\%$	$(0.82 \pm 0.15)\%$		[20]
$\mathcal{B}(f_2 \rightarrow K\bar{K})$	$(4.6 \pm 0.4)\%$	$(88.7 \pm 2.2)\%$		[20]
$\mathcal{B}(f_2 \rightarrow \eta\eta)$	$(4.0 \pm 0.8) \times 10^{-3}$	$(10.4 \pm 2.2)\%$		[20]
$\mathcal{B}(f_2 \rightarrow \gamma\gamma)$	$(1.64 \pm 0.19) \times 10^{-5}$	$(1.11 \pm 0.14) \times 10^{-6}$		[20]
r_R	3.62 ± 0.03	3.62 ± 0.03	(GeV/ c) $^{-1}$	[2]

$f_2'(1525)$, $f_2(1810)$, and $f_2(1950)$], the energy-dependent total width $\Gamma_{\text{tot}}(W)$ is given by

$$\Gamma_{\text{tot}}(W) = \sum_X \Gamma_{X\bar{X}}(W), \quad (7)$$

where X is a π , K , η , γ , etc. The partial width $\Gamma_{X\bar{X}}(W)$ is parameterized as [25]

$$\Gamma_{X\bar{X}}(W) = \Gamma_R \mathcal{B}(R \rightarrow X\bar{X}) \left(\frac{q_X(W^2)}{q_X(m_R^2)} \right)^5 \frac{D_2(q_X(W^2)r_R)}{D_2(q_X(m_R^2)r_R)}, \quad (8)$$

where Γ_R is the total width at the resonance mass, $q_X(W^2) = \sqrt{W^2/4 - m_X^2}$, $D_2(x) = 1/(9 + 3x^2 + x^4)$, and r_R is an effective interaction radius that varies from 1 to 7 GeV $^{-1}$ in different hadronic reactions [26]. We assume the same r_R value from Ref. [2] for $f_2(1270)$ and $f_2'(1525)$.

For the 4π and other decay modes, $\Gamma_{4\pi}(W) = \Gamma_R \mathcal{B}(R \rightarrow 4\pi) \frac{W^2}{m_R^2}$ is used instead of Eq. (8) for $f_2(1270)$. Parameters of $f_2(1270)$ and $f_2'(1525)$ are summarized in Table IV. The resonance parameters given in Ref. [20] for $f_0(1370)$ and $f_0(1500)$ are summarized in Table V. Background amplitudes are parameterized as follows:

$$\begin{aligned} B_S &= \beta(b_S(W - W_0) + c_S), \\ B_{D0} &= \beta^5(b_0(W - W_0) + c_0), \\ B_{D2} &= \beta^5(b_2(W - W_0) + c_2), \end{aligned}$$

where β is the velocity of the η meson in the c.m. and $W_0 = 2m_\eta$. We set $B_{D0} = 0$, that is, $b_0 = c_0 = 0$, in the nominal fit. We assume the background amplitudes for S and D_2 to be real and linear in W to reduce the number of parameters. Furthermore, we fix arbitrary phases by choosing $c_S > 0$ and $c_2 > 0$.

TABLE V. Parameters of $f_0(1370)$ and $f_0(1500)$ [20].

Parameter	$f_0(1370)$	$f_0(1500)$	Unit
Mass	1200–1500	1505 ± 6	MeV/ c^2
Width	150–250	109 ± 7	MeV
$\mathcal{B}(\eta\eta)$	Seen	$(5.1 \pm 0.9)\%$	
$\mathcal{B}(\gamma\gamma)$	Unknown	Unknown	

We fit the energy region of $1.12 \text{ GeV} < W < 1.64 \text{ GeV}$. In the fit, we fix the values of the parameters of $f_2(1270)$ and $f_2'(1525)$ to those in the PDG [20] except for the product $\Gamma_{\gamma\gamma} \mathcal{B}(\eta\eta)$ for $f_2(1270)$.

Two hundred sets of randomly generated initial parameters are prepared and fits are performed for each study. A unique solution is obtained with a fit quality of $\chi^2/\text{ndf} = 137.1/119$, where ndf is the number of degrees of freedom in the fit. A fit without $f_0(Y)$ gives a poor fit with $\chi^2/\text{ndf} = 209.7/123$. The parameters obtained from these two fits are summarized in Table VI. The product $\Gamma_{\gamma\gamma} \mathcal{B}(\eta\eta)$ for $f_2(1270)$ is $11.5^{+1.8}_{-2.0}$ eV and is consistent with 12.1 ± 2.8 eV in the PDG [20]. Figures 10–12 show results of the nominal fit to differential cross sections, the total cross section, and spectra of \hat{S}^2 , \hat{D}_0^2 , and \hat{D}_2^2 .

Fits where the value of the product $\Gamma_{\gamma\gamma} \mathcal{B}(\eta\eta)$ of $f_2'(1525)$ is floated while that of $f_2(1270)$ is fixed to the PDG value yield three solutions listed in Table VII. Thus we fix the former to the PDG values in further studies.

The following sources of systematic errors on the parameters are considered: dependence on the fitted region, normalization errors of the differential cross sections, assumptions on the background amplitudes, and the measurement errors of $f_2(1270)$ and $f_2'(1525)$.

For each study, a fit is made allowing all the parameters to float; the differences of the fitted parameters from the

TABLE VI. Fitted parameters for the nominal fit and for a fit without $f_0(Y)$ in the low mass region.

Parameter	Nominal	Without $f_0(Y)$	Unit
Mass ($f_0(Y)$)	1262^{+51}_{-78}	...	MeV/ c^2
Width ($f_0(Y)$)	484^{+246}_{-170}	...	MeV
$\Gamma_{\gamma\gamma} \mathcal{B}(\eta\eta)(f_0(Y))$	121^{+133}_{-53}	0 (fixed)	eV
ϕ_Y	38^{+19}_{-30}	–	deg.
$\Gamma_{\gamma\gamma} \mathcal{B}(\eta\eta)(f_2(1270))$	$11.5^{+1.8}_{-2.0}$	$11.7^{+1.4}_{-1.5}$	eV
ϕ_2	68^{+7}_{-5}	66 ± 4	deg.
ϕ_5	150^{+14}_{-12}	164 ± 13	deg.
b_S	$-2.9^{+3.2}_{-3.5}$	$-8.5^{+0.3}_{-0.4}$	$\sqrt{\text{nb}}/\text{GeV}$
c_S	$2.3^{+2.3}_{-1.8}$	3.7 ± 0.1	$\sqrt{\text{nb}}$
b_2	$6.5^{+7.6}_{-5.7}$	$-3.9^{+3.6}_{-4.5}$	$\sqrt{\text{nb}}/\text{GeV}$
c_2	$1.8^{+3.5}_{-4.6}$	$6.9^{+3.0}_{-2.3}$	$\sqrt{\text{nb}}$
$\chi^2(\text{ndf})$	137.1 (119)	209.7 (123)	...

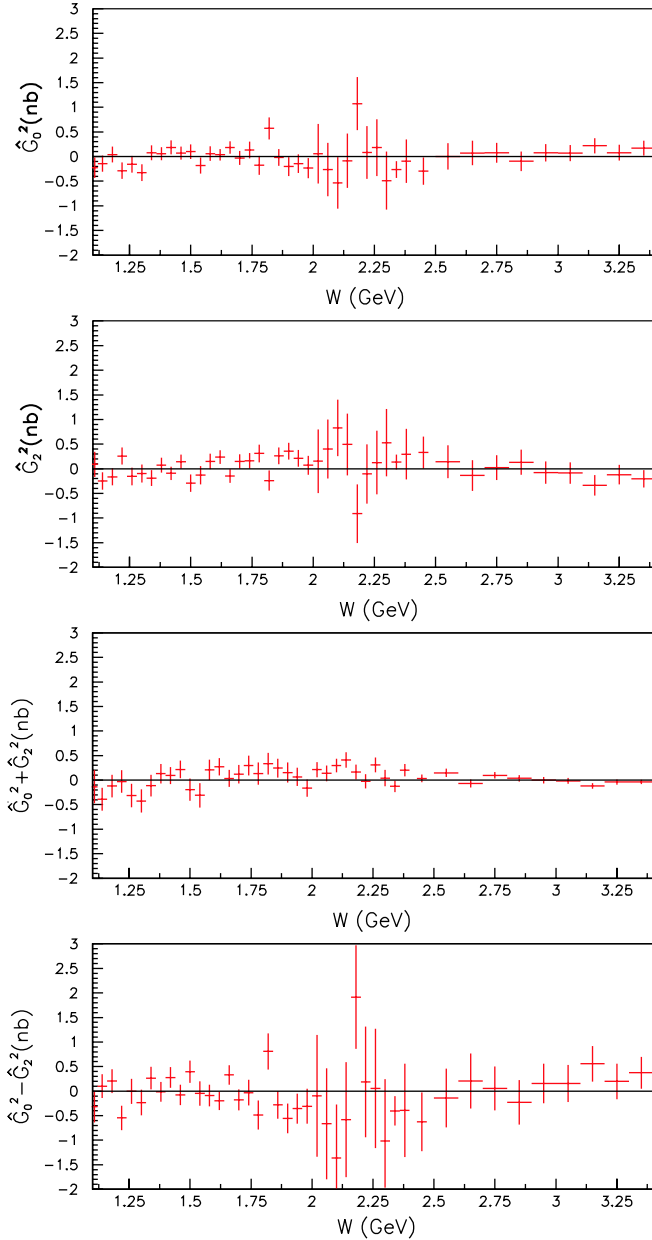


FIG. 9 (color online). Spectra of \hat{G}_0^2 , \hat{G}_2^2 , and $\hat{G}_0^2 \pm \hat{G}_2^2$. The error bars shown are statistical errors that do not include correlations.

nominal values are quoted as systematic errors. Here too, two hundred sets of randomly generated initial parameters are prepared for each study and fitted to search for the true minimum and for possible multiple solutions. Unique solutions are found many times. Once a solution is found, several more iterations of the fitting procedure are made to confirm the convergence.

The resulting systematic errors are summarized in Table VIII. Two fitting regions are tried: one region that is shifted lower by one bin ($1.08 \text{ GeV} \leq W \leq 1.60 \text{ GeV}$) and another shifted higher by one bin ($1.16 \text{ GeV} \leq W \leq 1.68 \text{ GeV}$). Studies on normalization are divided into those

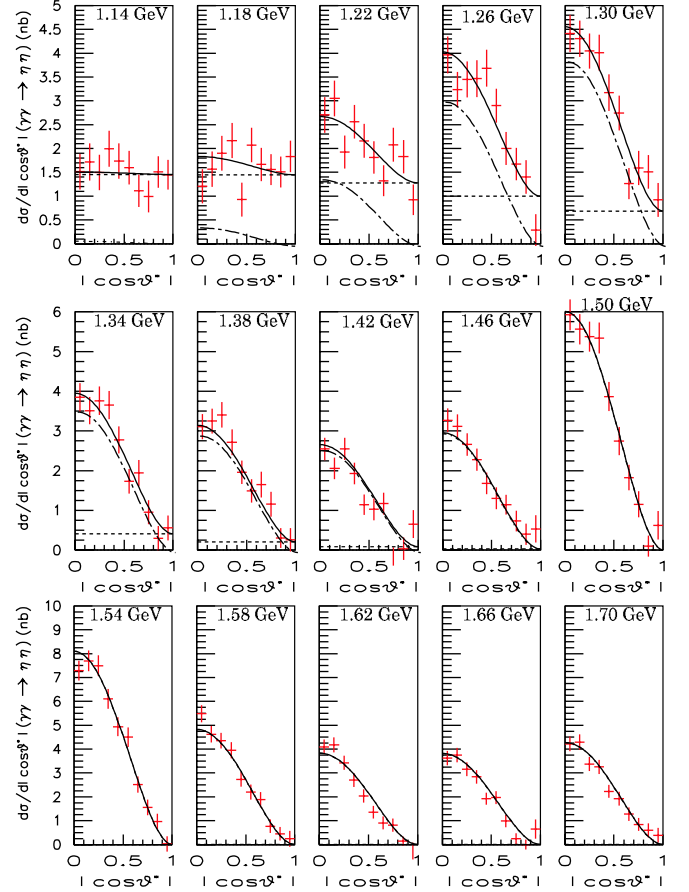


FIG. 10 (color online). Differential cross sections (points with error bars) and fitted curves for the nominal fit in the low mass region (solid curve). Dotted (dot-dashed) curves are $|S|^2$ ($|D_2|^2$) from the fit. The vertical error bars are statistical only.

from uncertainties of the overall normalization and those from distortion of the spectra in either $|\cos\theta^*|$ or W . For overall normalization errors, fits are made with two sets of values of differential cross sections obtained by multiplying by $(1 \pm \sigma_\epsilon(W, |\cos\theta^*|))$, where σ_ϵ is the relative efficiency error; they are denoted as “normalization \pm ” in the table. For distortion studies, $\pm 4\%$ errors for $|\cos\theta^*| < 1$ and $\pm 4\%/ \text{GeV}$ for the W dependence are assigned, based on the uncertainty discussed for (9) in Sec. IV E. Differential cross sections are modified by multiplying by $(1 \pm 0.08|\cos\theta^*| \mp 0.04)$ and $(1 \pm 0.08(W [\text{GeV}] - 1.38))$ (denoted as “bias: $|\cos\theta^*| \pm$ ” and “bias: $W \pm$ ”, respectively). For studies of background (BG) amplitudes, either b_i or c_i is set to zero for B_S and B_{D_2} , while either b_0 or c_0 is floated for B_{D_0} . Finally, the parameters of $f_2(1270)$ and $f_2'(1525)$ and the value of r_R are successively varied by their errors.

The total systematic errors are calculated by adding individual errors in quadrature. As can be seen in Table VIII, we obtain

$$\Gamma_{\gamma\gamma} \mathcal{B}(f_2(1270) \rightarrow \eta\eta) = 11.5^{+1.8}_{-2.0} {}^{+4.5}_{-3.7} \text{ eV}, \quad (9)$$

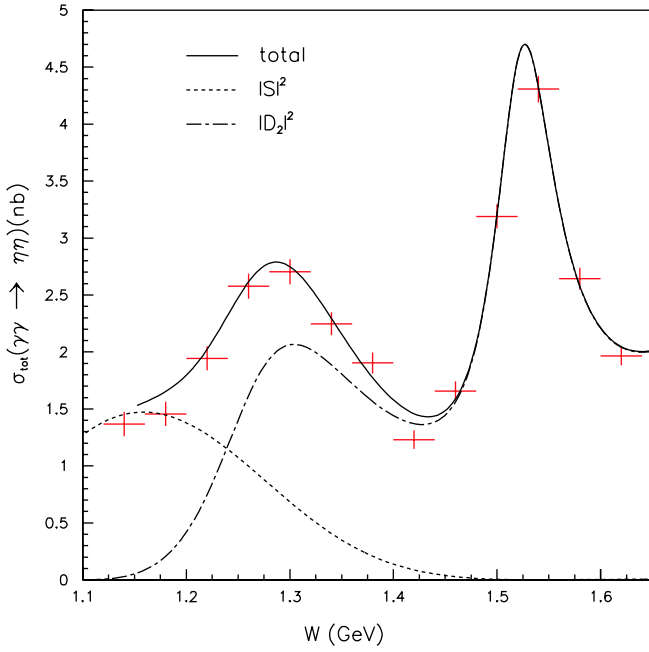


FIG. 11 (color online). Total cross section (points with error bars) ($|\cos\theta^*| < 1.0$) and fitted curves for the nominal fit in the low mass region (solid curve). Dotted (dot-dashed) curves are $|S|^2$ ($|D_2|^2$) from the fit. The vertical errors are statistical only.

which is consistent with previous measurements [20]. The apparent threshold enhancement in the S wave is fitted in terms of a scalar meson $f_0(Y)$, whose mass, width, and $\Gamma_{\gamma\gamma}\mathcal{B}(\eta\eta)$ are obtained to be

$$M_{f_0(Y)} = 1262^{+51}_{-78} {}^{+82}_{-103} \text{ MeV}/c^2, \quad (10)$$

$$\Gamma_{f_0(Y)} = 484^{+246}_{-170} {}^{+246}_{-263} \text{ MeV}, \quad (11)$$

$$\Gamma_{\gamma\gamma}\mathcal{B}(f_0(Y) \rightarrow \eta\eta) = 121^{+133}_{-53} {}^{+169}_{-106} \text{ eV}, \quad (12)$$

respectively.

The mass peak of the $f_0(Y)$ does not coincide with the broad peak in the \hat{S}^2 spectrum in Fig. 12 due to the effects of interference.

2. Higher mass region, up to 2.0 GeV

Now we investigate the higher mass region. We fix most of the parameters determined at lower energy and introduce, just for the purpose of parameterization, a single tensor resonance $f_2(X)$, whose mass, width, and $\Gamma_{\gamma\gamma}\mathcal{B}(\eta\eta)$ are left free and fit the region $1.16 \text{ GeV} < W < 2.0 \text{ GeV}$. We parameterize partial waves as follows:

$$\begin{aligned} S &= A_{f_0(Y)} e^{i\phi_Y} + B_S e^{i\phi_S}, & D_0 &= B_{D0}, \\ D_2 &= A_{f_2(1270)} e^{i\phi_2} + A_{f_2(1525)} e^{i\phi_5} + A_{f_2(X)} e^{i\phi_X} + B_{D2}, \end{aligned} \quad (13)$$

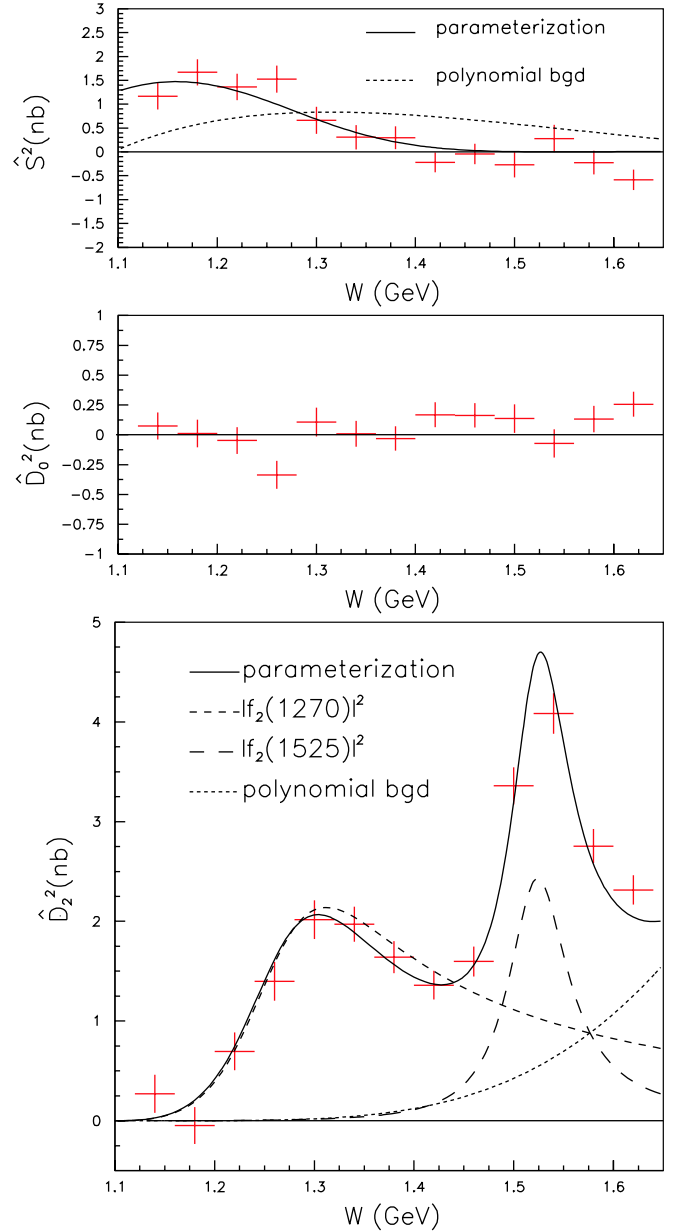


FIG. 12 (color online). \hat{S}^2 , \hat{D}_0^2 , and \hat{D}_2^2 and fitted curves for the nominal fit in the low mass region (solid curve). The points with error bars are the results of the W -independent fits (the same as those in Fig. 8). The vertical error bars are statistical only.

where $A_{f_0(Y)}$, $A_{f_2(1270)}$, and $A_{f_2(1525)}$ are fixed at the values that are fitted in the low mass region. Here too, B_{D0} is set to zero and B_S is fixed at the values found above. The phases ϕ_Y , ϕ_2 , and ϕ_5 are also fixed and $\phi_S = 0$. Only the b_2 and c_2 parameters of B_{D2} are floated along with the parameters of $f_2(X)$, i.e., its mass, width, $\Gamma_{\gamma\gamma}\mathcal{B}(\eta\eta)$, and ϕ_X .

Two hundred sets of randomly generated initial parameters are prepared and fits are performed for each study. A unique solution is obtained with a fit quality of $\chi^2/\text{ndf} = 311.4/204$. The parameters obtained are summarized in Table IX. Figures 13–15 show results of the nominal fit to

TABLE VII. Three solutions obtained when $\Gamma_{\gamma\gamma}\mathcal{B}(\eta\eta)(f'_2(1525))$ is floated in fits to the low mass region.

Parameter	Sol. A	Sol. B	Sol. C	Unit
Mass ($f_0(Y)$)	1259^{+50}_{-79}	1259^{+54}_{-80}	1264^{+55}_{-86}	MeV/ c^2
Width ($f_0(Y)$)	471^{+234}_{-169}	502^{+241}_{-191}	536^{+261}_{-193}	MeV
$\Gamma_{\gamma\gamma}\mathcal{B}(\eta\eta)(f_0(Y))$	116^{+122}_{-52}	127^{+139}_{-59}	143^{+162}_{-69}	eV
ϕ_Y	36^{+20}_{-31}	38^{+19}_{-32}	41^{+18}_{-30}	deg.
$\Gamma_{\gamma\gamma}\mathcal{B}(\eta\eta)(f'_2(1525))$	$23.1^{+2.6}_{-2.8}$	$8.0^{+2.0}_{-1.5}$	$5.0^{+5.8}_{-5.0}$	eV
ϕ_2	4^{+10}_{-9}	68^{+10}_{-11}	45^{+23}_{-21}	deg.
ϕ_5	188^{+17}_{-14}	155^{+10}_{-11}	94 ± 22	deg.
b_S	$-2.9^{+3.2}_{-3.7}$	$-2.9^{+3.2}_{-3.7}$	$-2.9^{+3.2}_{-3.6}$	$\sqrt{\text{nb}}/\text{GeV}$
c_S	$2.3^{+2.4}_{-1.9}$	$2.3^{+1.7}_{-1.9}$	$2.4^{+2.6}_{-1.9}$	$\sqrt{\text{nb}}$
b_2	$1.5^{+6.0}_{-4.8}$	$3.8^{+6.4}_{-1.9}$	$-12.5^{+2.5}_{-2.4}$	$\sqrt{\text{nb}}/\text{GeV}$
c_2	$5.2^{+2.8}_{-3.2}$	3.2 ± 1.2	$5.8^{+1.1}_{-1.2}$	$\sqrt{\text{nb}}$
$\chi^2(\text{ndf})$	136.4 (119)	137.2 (119)	138.6 (119)	...

the differential cross sections, the total cross section, and spectra of \hat{S}^2 , \hat{D}_0^2 , and \hat{D}_2^2 . A more sophisticated parameterization results in multiple solutions. As an example, two solutions are found when the parameters of B_S are also floated; these are also listed in Table IX. Hence we employ the simple parameterization given in Eq. (13). This parameterization results in discrepancies from the fits in some W regions for differential and integrated cross sections.

Various sources of the systematic errors are studied and evaluated using various fits similar to those applied in the analysis for the low mass region, as summarized in Table X. We take into account the errors for the $f_0(Y)$ parameters, as well as those for $f_2(1270)$ and $f'_2(1525)$. We try two fitting regions shifted lower by two bins ($1.08 \text{ GeV} \leq W \leq 1.92 \text{ GeV}$) and higher by two bins ($1.24 \text{ GeV} \leq W \leq 2.08 \text{ GeV}$). For studies of BG amplitudes, either c_2 or b_2 is set to zero for B_{D_2} or allowed to

float for B_{D_0} . The values of c_S and b_S are changed by their errors.

The total systematic errors are calculated by adding the individual errors in quadrature. The mass, width, and $\Gamma_{\gamma\gamma}\mathcal{B}(\eta\eta)$ obtained for the $f_2(X)$ meson are

$$M_{f_2(X)} = 1737 \pm 9^{+198}_{-65} \text{ MeV}/c^2, \quad (14)$$

$$\Gamma_{f_2(X)} = 228^{+21}_{-20} \text{ }^{+234}_{-153} \text{ MeV}, \quad (15)$$

$$\Gamma_{\gamma\gamma}\mathcal{B}(f_2(X) \rightarrow \eta\eta) = 5.2^{+0.9}_{-0.8} \text{ }^{+37.3}_{-4.5} \text{ eV}, \quad (16)$$

respectively.

The rather poor χ^2 of the fit and the clear disagreement in Figs. 14 and 15 above $f'_2(1525)$ may imply that more than one tensor resonance exists in this mass region. Unfortunately, we cannot draw any definite conclusions about such a possibility from additional fits to the data,

TABLE VIII. Systematic uncertainties for the fit in the low mass region.

Source	Mass (MeV/ c^2)	$f_0(Y)$ Γ_{tot} (MeV)	$\Gamma_{\gamma\gamma}\mathcal{B}(\eta\eta)$ (eV)	$f_2(1270)$ $\Gamma_{\gamma\gamma}\mathcal{B}_{\eta\eta}$ (eV)
W range	+56.5	+0.0	+26.9	+0.4
Bias: W	-8.9	-17.8	-17.0	-1.1
Bias: $ \cos\theta^* $	+1.1	+1.2	+2.3	+0.1
Normalization	-1.7	0.0	-2.1	-0.1
BG: B_S	+0.1	+0.5	+0.6	+0.1
BG: D_0	-0.5	-0.8	-0.9	-0.1
BG: D_2	+27.0	+220.9	+152.1	+3.0
f_2 mass	-48.8	-199.1	-87.1	-2.4
f_2 width	+0.0	+0.0	+0.0	+0.0
f'_2 mass	-84.9	-162.9	-54.3	-0.0
f'_2 width	+49.6	+0.0	+37.3	+0.0
r_R	-0.0	-42.1	-0.0	-2.0
Total	+4.6	+100.1	+30.4	+1.9
	-10.1	-26.7	-6.0	-0.8
	+0.4	+4.1	+2.0	+0.3
	-0.2	-2.5	-1.4	-0.3
	+1.1	+0.4	+1.3	+0.2
	-0.4	-0.0	-0.5	-0.2
	+8.7	+41.5	+21.1	+2.2
	-24.7	-0.0	-20.3	-1.4
	+4.8	+2.5	+0.5	+0.3
	-5.6	-8.4	-2.7	-0.4
	+13.0	+11.7	+13.0	+1.5
	-13.7	-0.0	-6.6	-0.4
	+0.2	+0.6	+0.2	+0.0
	-0.2	-1.5	-0.4	-0.0
	+81.7	+246.4	+169.4	+4.5
	-103.0	-262.8	-106.4	-3.7

TABLE IX. Fitted parameters for the nominal fit and results obtained when the B_S parameters are floated for the high mass region.

Parameter	Nominal	Free B_S		Unit
		Sol. A	Sol. B	
Mass ($f_2(X)$)	1737 ± 9	1742 ± 10	1738 ± 9	MeV/c^2
Width ($f_2(X)$)	228^{+21}_{-20}	223^{+23}_{-22}	236^{+21}_{-20}	MeV
$\Gamma_{\gamma\gamma}\mathcal{B}(\eta\eta)(f_2(X))$	$5.2^{+0.9}_{-0.8}$	$4.7^{+1.0}_{-0.9}$	$6.0^{+1.2}_{-1.0}$	eV
ϕ_X	159^{+6}_{-5}	160^{+7}_{-6}	154 ± 5	deg.
b_S	-2.9 (fixed)	4.4 ± 0.3	-2.8 ± 0.3	$\sqrt{\text{nb}/\text{GeV}}$
c_S	2.3 (fixed)	0.9 ± 0.2	1.8 ± 0.2	$\sqrt{\text{nb}}$
b_2	-8.1 ± 0.7	$-9.1^{+0.8}_{-0.9}$	-9.9 ± 0.9	$\sqrt{\text{nb}/\text{GeV}}$
c_2	9.4 ± 0.5	$9.8^{+0.6}_{-0.5}$	10.4 ± 0.6	$\sqrt{\text{nb}}$
$\chi^2(\text{ndf})$	311.4 (204)	279.3 (202)	288.8 (202)	...

because interference between amplitudes introduces too much additional freedom.

VI. ANALYSIS OF THE HIGH ENERGY REGION ABOVE 2.4 GEV

In this section, we present a study of the angular dependence of the differential cross section, the W dependence of the total cross section, the ratio of cross sections for $\eta\eta$ to $\pi^0\pi^0$, and χ_{cJ} charmonium production in the high energy region $W > 2.4$ GeV.

A. Angular dependence

As in the analysis of the $\pi^0\pi^0$ [11] and $\eta\pi^0$ [12] processes, we compare the angular dependence of the

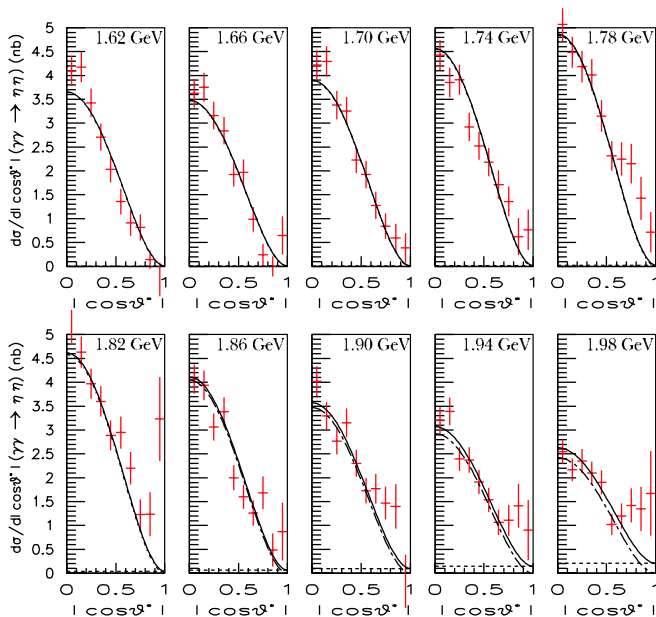


FIG. 13 (color online). Differential cross sections (points with error bars) in the energy bins indicated and fitted curves for the nominal fit in the high mass region (solid curve). Dotted (dot-dashed) curves are $|S|^2$ ($|D_2|^2$) from the fit. The vertical error bars are statistical only.

differential cross sections with the function $1/\sin^4\theta^*$ for the data in the W range $2.4 \text{ GeV} < W < 3.3 \text{ GeV}$.

In the study of $\pi^0\pi^0$ data, the contribution from the charmonia is subtracted [11]. However, no reliable charmonium subtraction is possible for the $\eta\eta$ cross section because of the low statistics and the larger charmonium component (see Sec. IV D) compared to the $\pi^0\pi^0$ case. We limit our discussion in Secs. VIA, VIB, and VIC to the region $W < 3.3$ GeV only, where the contribution of charmonium is small.

Figure 16 compares the normalized differential cross sections with the function $0.322/\sin^4\theta^*$ (solid curves). The factor in the numerator is calculated by dividing differential cross sections, which are proportional to

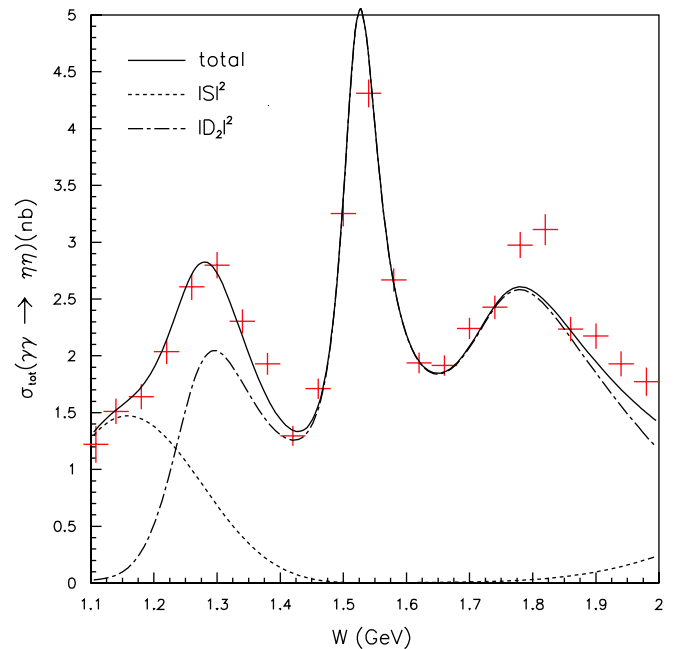


FIG. 14 (color online). Total cross sections (points with error bars) ($|\cos\theta^*| < 1.0$) and fitted curves for the nominal fit in the high mass region (solid curve). Dotted (dot-dashed) curves are $|S|^2$ ($|D_2|^2$) from the fit. The vertical error bars are statistical only.

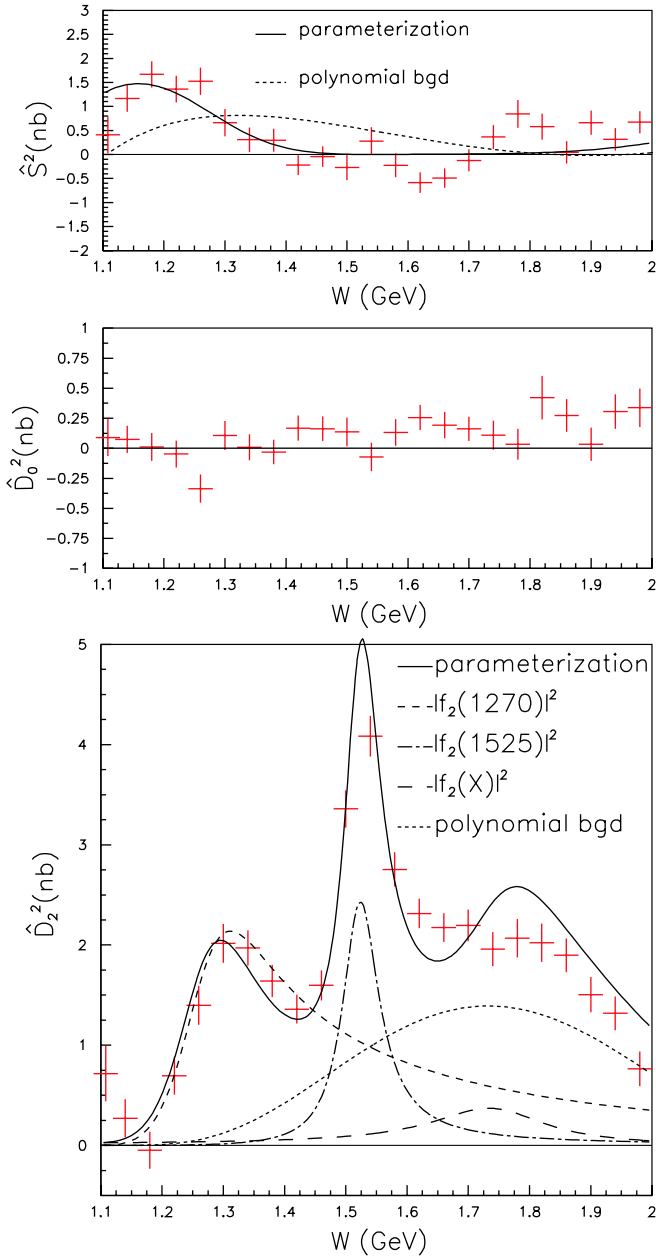


FIG. 15 (color online). \hat{S}^2 , \hat{D}_0^2 , and \hat{D}_2^2 and fitted curves for the nominal fit in the high mass region (solid curve). The points with error bars are the results of the W -independent fits (the same as those in Fig. 8). The vertical error bars are statistical only.

$1/\sin^4\theta^*$ by the total integral for $|\cos\theta^*| < 0.9$. Agreement is poor in the W region considered. A $1/\sin^6\theta^*$ dependence (dashed curves in the same figure) agrees better with the data for $W > 3.0$ GeV. The χ^2 's for the $1/\sin^4\theta^*$ ($1/\sin^6\theta^*$) dependences are 29.6 (14.3) for the $W = 3.05$ GeV bin, 27.8 (7.8) for the $W = 3.15$ GeV bin, and 9.8 (4.7) for the $W = 3.25$ GeV bin. The number of degrees of freedom is 8, and only statistical errors are used to evaluate the χ^2 .

A $1/\sin^4\theta^*$ dependence is not a prediction of perturbative QCD (pQCD) for neutral-meson-pair production, and

thus the disagreement does not imply an inconsistency with the pQCD model [14]. However, it might indicate that the $\eta\eta$ production mechanism is different from that of $\pi^0\pi^0$ and other production processes where a $1/\sin^4\theta^*$ dependence describes data well for $W > 3.1$ GeV. The handbag model also predicts a $1/\sin^4\theta^*$ dependence for neutral-meson-pair production processes at large Mandelstam variable t [15,16]. These predictions are critically discussed in Ref. [27].

B. W^{-n} dependence

We fit the W^{-n} dependence of the total cross section ($|\cos\theta^*| < 0.8$, where we take the upper boundary 0.8, to match that in our $\pi^0\pi^0$ analysis) in the energy region 2.4–3.3 GeV. The fit gives

$$n = 7.8 \pm 0.6(\text{stat}) \pm 0.4(\text{sys}), \quad (17)$$

and the corresponding cross section is shown in Fig. 17(a) together with that of the $\pi^0\pi^0$ process in the same angular range.

The systematic error is obtained by simultaneously varying the cross section by $\pm 1\sigma$ at 2.45 GeV and $\mp 1\sigma$ at 3.25 GeV and by $\mp(W [\text{GeV}] - 2.85)\sigma/0.4$ for the other W points in between, where σ , amounting to 6%, is the systematic error that does not include the uncertainty in the energy-independent normalization.

The slope parameter n can be compared with n values in other processes that we have studied earlier [3,5,11,12].

TABLE X. Systematic uncertainties for the fit in the high mass region.

Source	$f_2(X)$		
	Mass (MeV/ c^2)	Γ_{tot} (MeV)	$\Gamma_{\gamma\gamma}\mathcal{B}(\eta\eta)$ (eV)
W range	+95.0	+38.8	+3.4
Bias: W	+0.0	-101.8	+1.5
Bias: $ \cos\theta^* $	+3.8	+14.2	+0.6
Normalization	-3.8	-13.0	-0.5
BG: c_S	+0.7	+6.1	+0.4
BG: b_S	-0.8	-6.1	-0.3
BG: B_{D0}	+125.5	+142.7	+16.7
f_2 mass	-10.4	-0.0	-0.0
f_2 width	+0.0	+0.0	+0.0
$f_2 \Gamma_{\gamma\gamma}\mathcal{B}(\eta\eta)$	+0.0	+0.0	+0.0
ϕ_2	-1.4	-6.2	-0.5
f_2^I mass	+1.0	+4.7	+0.2
f_2^I width	-1.1	-4.8	-0.2
$f_2^I \Gamma_{\gamma\gamma}\mathcal{B}(\eta\eta)$	+1.1	+5.1	+0.2
ϕ_2^I	-1.4	-4.1	-0.2
f_2^{II} mass	+0.0	+60.6	+4.2
f_2^{II} width	-8.2	-0.0	-0.4
$f_2^{II} \Gamma_{\gamma\gamma}\mathcal{B}(\eta\eta)$	+5.1	+11.8	+0.4
ϕ_2^{II}	-9.4	-7.5	-0.6
f_2^{III} mass	+3.8	+10.4	+0.6
f_2^{III} width	-32.4	-7.2	-0.4
$f_2^{III} \Gamma_{\gamma\gamma}\mathcal{B}(\eta\eta)$	+6.0	+7.2	+0.4
ϕ_2^{III}	-5.9	-8.1	-0.4
f_2^{IV} mass	+30.4	+4.5	+0.6
f_2^{IV} width	-32.4	-0.0	-0.0
$f_2^{IV} \Gamma_{\gamma\gamma}\mathcal{B}(\eta\eta)$	+9.4	+24.2	+0.2
ϕ_2^{IV}	-13.3	-15.2	-0.0
$f_0(Y)$ mass	+14.0	+93.3	+6.3
$f_0(Y)$ width	-21.8	-41.1	-1.9
$f_0(Y) \Gamma_{\gamma\gamma}\mathcal{B}(\eta\eta)$	+36.4	+70.3	+3.9
$f_0(Y)$ phase	-18.2	-79.7	-2.7
r_R	+27.0	+76.2	+4.6
Total	-20.0	-66.3	-2.5
	+105.7	+91.8	+31.7
	-21.5	-0.0	-0.0
	+0.5	+0.9	+0.0
	-0.6	-0.8	-0.0
	+198.3	+233.7	+37.3
	-65.3	-153.1	-4.5

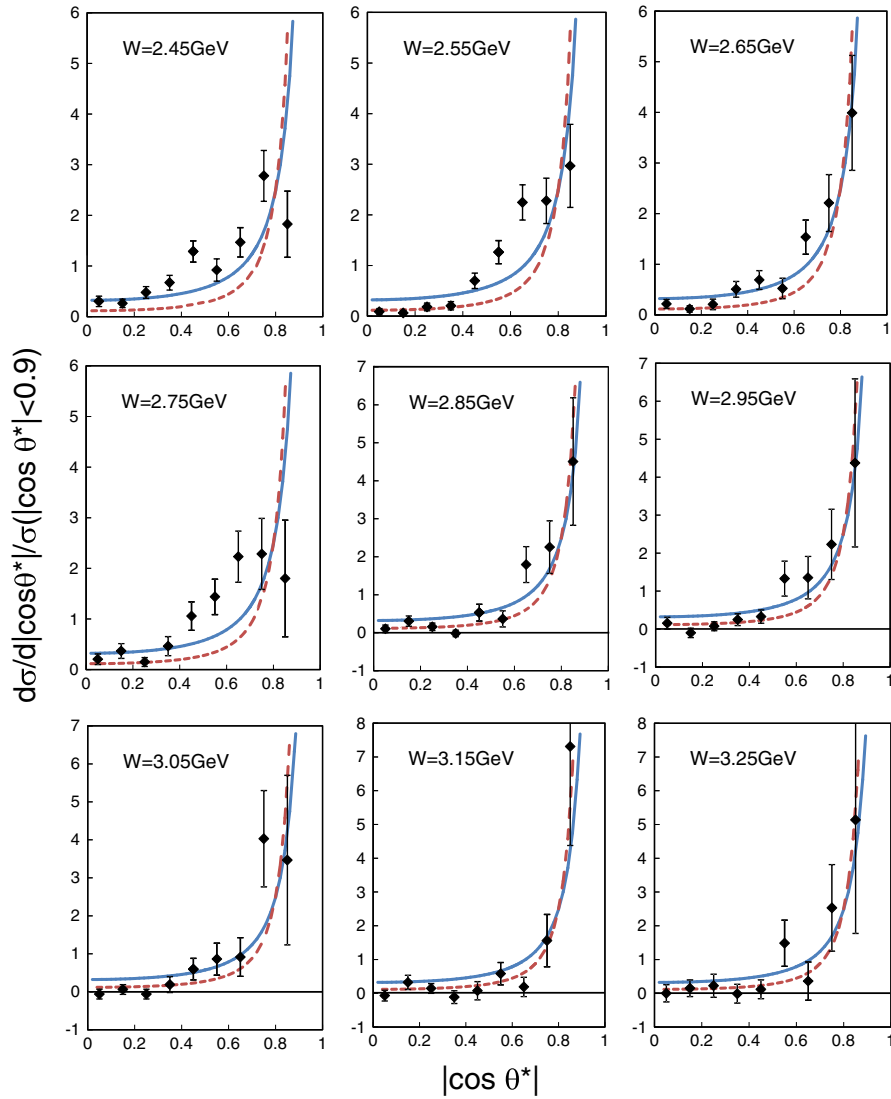


FIG. 16 (color online). The angular dependence of the differential cross sections in different W regions, with the normalization to the cross section integrated over $|\cos\theta^*| < 0.9$. The solid and dashed curves are proportional to $1/\sin^4\theta^*$ and $1/\sin^6\theta^*$, respectively, normalized similarly.

The results are summarized in Table XI. The present value for the $\eta\eta$ process is close to that for the $\pi^0\pi^0$ process, although we note the measured W regions are different. Differences in this parameter among different processes are discussed in Ref. [27].

C. Cross section ratio

The ratio of cross sections between neutral-pseudoscalar-meson (π^0 or η) pairs in two-photon collisions can be predicted relatively reliably in both pQCD and handbag models, based on quark charges and flavor-SU(3) symmetry. The pQCD model [14] predictions for the cross section ratios for $\pi^0\pi^0$, $\eta\pi^0$, and $\eta\eta$ are summarized in Table XII. In the table, $R_f = (f_\eta/f_{\pi^0})^2$, where f_η (f_π) is the η (π^0) form factor. The value of R_f is not well known,

and we provisionally assume it to be unity. The ratio of the cross sections is proportional to the square of the coherent sum of the product of the quark charges, $|\sum e_1 e_2|^2$, in which $e_1 = -e_2$ in the present neutral-meson production cases. We show two predictions: a pure flavor-SU(3) octet state and a mixture with $\theta_p = -18^\circ$ for the η and η' mesons. Here, we assume that the quark-antiquark component of the neutral-meson wave functions dominates and is much larger than the two-gluon component, in obtaining the relations between the cross sections.

The W dependence of the ratio between the measured cross section integrated over $|\cos\theta^*| < 0.8$ of $\gamma\gamma \rightarrow \eta\eta$ to $\gamma\gamma \rightarrow \pi^0\pi^0$ is plotted in Fig. 17(b). For the $\pi^0\pi^0$ process, the contributions from charmonium production are subtracted using a model-dependent assumption described in

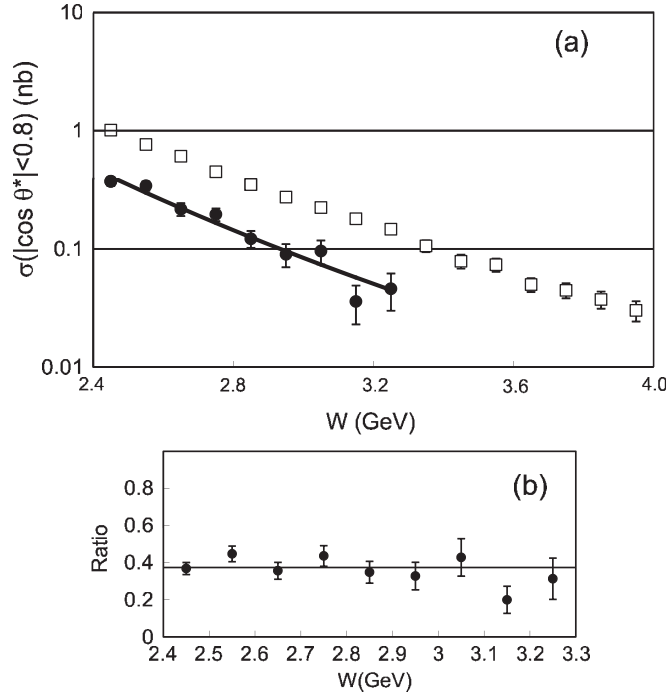


FIG. 17. (a) The W dependence of the cross sections ($|\cos\theta^*| < 0.8$) for the $\pi^0\pi^0$ (open squares) [11] and $\eta\eta$ (closed circles) processes. The curve is the power-law fit for the latter process. (b) The W dependence of the cross section ratio of $\eta\eta$ to $\pi^0\pi^0$ ($|\cos\theta^*| < 0.8$). The line is the average in the 2.4–3.3 GeV range. The error bars are only statistical in the above figures.

Ref. [11]. We use the $\eta\eta$ result only below $W < 3.3$ GeV, where the charmonium contribution is negligibly small. Even though the ratio may have a slight W dependence, in order to compare with QCD (as was done for other processes) we average the ratio of the cross sections over the range $2.4 \text{ GeV} < W < 3.3 \text{ GeV}$ and obtain

$$\frac{\sigma(\eta\eta)}{\sigma(\pi^0\pi^0)} = 0.37 \pm 0.02(\text{stat}) \pm 0.03(\text{sys}) \quad (18)$$

for $|\cos\theta^*| < 0.8$. The prediction of this model with $\theta_p = -18^\circ$ and $R_f = 1$ agrees well with our previous $\eta\pi^0$ measurement [12], but it is in poor agreement for the $\eta\eta$ process. However, we note that the W regions are different in the two cases.

The prediction of the $\eta\eta$ cross section for $|\cos\theta^*| < 0.6$ from the handbag model is presented in Fig. 5 in Ref. [16], which is based on measurements of other meson-pair production processes. We show the results from this measurement, which can be directly compared with the prediction in Table XIII. Agreement between the measurement and prediction is fairly good.²

²We do not give a quantitative comparison because Ref. [16] provides only a figure without any numerical values.

D. Extraction of χ_{cJ} charmonium contribution

As in our previous $\pi^0\pi^0$ analysis [11], we extract the contributions from the χ_{c0} and χ_{c2} charmonia from the $\eta\eta$ data, using the raw yield distribution in the region $2.8 \text{ GeV} < W < 3.8 \text{ GeV}$ integrated over $|\cos\theta^*| < 0.4$ (Fig. 18), where the contribution is enhanced against the forward peak from the QCD effect.

The same formula as in our analysis for the $\pi^0\pi^0$ final state [11] is used, where partial interference between the χ_{c0} charmonium and the continuum component is taken into account:

$$Y(W) = |\sqrt{\alpha k W^{-\beta}} + e^{i\phi} \sqrt{N_{\chi_{c0}}} \text{BW}_{\chi_{c0}}(W)|^2 + N_{\chi_{c2}} |\text{BW}_{\chi_{c2}}(W)|^2 + \alpha(1-k)W^{-\beta}, \quad (19)$$

where $\text{BW}_{\chi_{cJ}}(W)$ is a Breit-Wigner function for the charmonium amplitude, which is proportional to $\sim 1/(W^2 - M_{\chi_{cJ}}^2 - iM_{\chi_{cJ}}\Gamma_{\chi_{cJ}})$ and is normalized as $\int |\text{BW}_{\chi_{cJ}}(W)|^2 dW = 1$. The masses and widths M and Γ , respectively, of the charmonium states are fixed to the PDG world averages [20]. The component $\alpha W^{-\beta}$ corresponds to the contribution from the continuum, with a fraction k that interferes with the χ_{c0} amplitude with a relative phase angle ϕ .

We do fits with and without interference between the χ_{c0} and the continuum. The interference with χ_{c2} is neglected because of its narrow width. We assume a W resolution to be $0.01W$ from the MC simulation and take it into account in the fit by smearing the function $Y(W)$. We apply a binned maximum likelihood fit with a bin width $\Delta W = 20$ MeV.

The result with interference gives nearly the same result as the fit without interference but with larger errors. The fit with interference cannot determine the interference parameters k and ϕ with a useful accuracy. Therefore, we take the nominal result from the fit without interference. The best fit is shown in Fig. 18. The results are tabulated in Table XIV. Significances for the charmonium signals are 5.2σ for χ_{c0} and 3.0σ for χ_{c2} . The significances are obtained from the difference of the logarithmic likelihoods with and without the corresponding charmonium contribution, where the change in the number of degrees of freedom is taken into account. Here, in order to obtain the most conservative value, we extracted the value in the interference (noninterference) case for the χ_{c0} (χ_{c2}). The systematic errors are from uncertainties in the W scale and the W resolution (we vary them by ± 3 MeV and by $\pm 20\%$, respectively) and the efficiency error.

The results for $\Gamma_{\gamma\gamma}(\chi_{cJ})\mathcal{B}(\chi_{cJ} \rightarrow \eta\eta)$ are consistent with the product of the known total widths [20] and the branching fractions from the recent CLEO and BES measurements [28,29] (8.0 ± 0.9) and (0.30 ± 0.04) eV for χ_{c0} and χ_{c2} , respectively, where we take the average of the CLEO and BES measurements.

TABLE XI. The value of n in $\sigma_{\text{tot}} \propto W^{-n}$ in various reactions fitted in the W and $|\cos\theta^*|$ ranges indicated. The first and second errors are statistical and systematic, respectively.

Process	n	W range (GeV)	$ \cos\theta^* $ range	Reference
$\eta\eta$	$7.8 \pm 0.6 \pm 0.4$	2.4–3.3	<0.8	This work
$\eta\pi^0$	$10.5 \pm 1.2 \pm 0.5$	3.1–4.1	<0.8	[12]
$\pi^0\pi^0$	$8.0 \pm 0.5 \pm 0.4$	3.1–4.1 (3.3–3.6 excluded)	<0.8	[11]
$K_S^0 K_S^0$	$10.5 \pm 0.6 \pm 0.5$	2.4–4.0 (3.3–3.6 excluded)	<0.6	[5]
$\pi^+ \pi^-$	$7.9 \pm 0.4 \pm 1.5$	3.0–4.1	<0.6	[3]
$K^+ K^-$	$7.3 \pm 0.3 \pm 1.5$	3.0–4.1	<0.6	[3]

TABLE XII. Predictions and data for the cross section ratios [14] for $\pi^0\pi^0$, $\eta\pi^0$, and $\eta\eta$ production processes in two-photon collisions. Here, $R_f = (f_\eta/f_{\pi^0})^2$, where f_η (f_π) is the η (π^0) form factor; the value may be taken to be $R_f = 1$. The η meson is treated as a pure SU(3) octet state for the entries in the ‘‘octet’’ row, while ‘‘ $\theta_P = -18^\circ$ ’’ is the most probable mixing angle between the octet and singlet states from experiment [20]. The first and second errors for the data are statistical and systematic, respectively.

η in SU(3)	$\sigma(\eta\pi^0)/\sigma(\pi^0\pi^0)$	$\sigma(\eta\eta)/\sigma(\pi^0\pi^0)$
Octet	$0.24R_f$	$0.36R_f^2$
$\theta_P = -18^\circ$	$0.46R_f$	$0.62R_f^2$
Data (ref.)	$0.48 \pm 0.05 \pm 0.04$ [12]	$0.37 \pm 0.02 \pm 0.03$ (this work)
(W range)	(3.1 GeV $< W <$ 4.0 GeV)	(2.4 GeV $< W <$ 3.3 GeV)

TABLE XIII. Cross section integrated over $|\cos\theta^*| < 0.6$ multiplied by s^3 . The first and second errors are statistical and systematic, respectively.

s (GeV ²)	$s^3\sigma(\cos\theta^* < 0.6)$ (nb GeV ⁶)
6.00	$38.7 \pm 3.7 \pm 4.3$
6.50	$33.5 \pm 4.1 \pm 3.6$
7.02	$28.4 \pm 4.5 \pm 3.1$
7.56	$38.1 \pm 5.6 \pm 4.3$
8.12	$17.1 \pm 4.3 \pm 2.1$
8.70	$21.7 \pm 5.9 \pm 2.6$
9.30	$18.5 \pm 6.4 \pm 2.4$
9.92	$11.7 \pm 6.8 \pm 2.0$
10.56	$21.2 \pm 10.6 \pm 3.5$

VII. SUMMARY AND CONCLUSION

We have measured the cross section of $\gamma\gamma \rightarrow \eta\eta$ using a high-statistics data sample from e^+e^- collisions corresponding to an integrated luminosity of 393 fb^{-1} with the Belle detector at the KEKB accelerator. We obtain results for the differential cross sections in the center-of-mass energy (W) and polar-angle ($|\cos\theta^*|$) ranges of 1.096 GeV (the mass threshold) $< W < 3.8 \text{ GeV}$ and up to $|\cos\theta^*| = 0.9$ or 1.0 , depending on W .

The differential cross sections are fitted in the energy regions $1.12 \text{ GeV} < W < 1.64 \text{ GeV}$ and $1.20 \text{ GeV} < W < 2.00 \text{ GeV}$ using a simple parameterization of the S, D_0 , and D_2 waves, assuming that amplitudes consist of resonances and a smooth background. In the low energy fit, consistency of the parameters of $f_2(1270)$ and $f_2'(1525)$ with previous measurements is checked. The apparent threshold enhancement in the S wave is fitted in terms of a scalar meson $f_0(Y)$, whose mass, width, and

TABLE XIV. Charmonium yields and $\Gamma_{\gamma\gamma}\mathcal{B}(\eta\eta)$ from the present measurement. Two cases are shown: with and without interference between χ_{c0} and the continuum. The first and second (if given) errors are statistical and systematic, respectively. Only differences in log-likelihood values are meaningful.

Interference	Yield (χ_{c0})	Yield (χ_{c2})	$-2 \ln L/\text{ndf}$	$\Gamma_{\gamma\gamma}(\chi_{c0})\mathcal{B}(\chi_{c0} \rightarrow \eta\eta)$ (eV)	$\Gamma_{\gamma\gamma}(\chi_{c2})\mathcal{B}(\chi_{c2} \rightarrow \eta\eta)$ (eV)
Without	21.7 ± 5.3	8.5 ± 3.6	39.5/46	$9.4 \pm 2.3 \pm 1.2$	$0.53 \pm 0.22 \pm 0.09$
With	21.5 ± 9.2	10.1 ± 3.9	38.5/44		

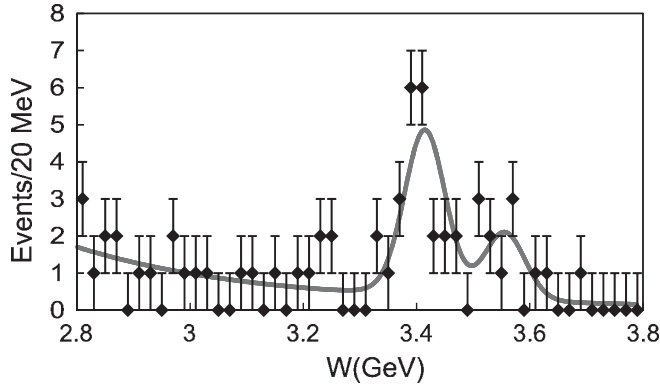


FIG. 18. The W distribution in the charmonium region ($|\cos\theta^*| < 0.4$). The fit does not take interference into account.

$\Gamma_{\gamma\gamma}\mathcal{B}(\eta\eta)$ are obtained to be $1262^{+51}_{-78} +^{82}_{-103}$ MeV/ c^2 , $484^{+246}_{-170} +^{246}_{-263}$ MeV, and $121^{+133}_{-53} +^{169}_{-106}$ eV, respectively. $f_0(Y)$ is introduced only to parameterize the data and may not be a single resonance.

For the energy region of $1.20 \text{ GeV} < W < 2.00 \text{ GeV}$, fits are then performed by fixing most of the parameters obtained in the low energy region and by including an additional tensor resonance. The obtained mass, width, and $\Gamma_{\gamma\gamma}\mathcal{B}(\eta\eta)$ for the tensor meson are $1737 \pm 9^{+198}_{-65}$ MeV/ c^2 , $228^{+21}_{-20} +^{234}_{-153}$ MeV, and $5.2^{+0.9}_{-0.8} +^{37.3}_{-4.5}$ eV, respectively. $f_2(X)$ is a parameterization used to describe the data in 1700 MeV mass region. It may represent some of the possible tensor resonances in this mass region.

We observe clear signals from $f_2(1270) \rightarrow \eta\eta$ and $f'_2(1525) \rightarrow \eta\eta$ for the first time in two-photon collisions. The product $\Gamma_{\gamma\gamma}\mathcal{B}(\eta\eta)$ for $f_2(1270)$ is $11.5^{+1.8}_{-2.0} +^{4.5}_{-3.7}$ eV. Our $f_2(X)$ may correspond to the $f_2(1810)$ state reported in Ref. [24]. The result of our measurements for the product $\Gamma_{\gamma\gamma}\mathcal{B}(\eta\eta)$ for $f_2(1270)$ and $f'_2(1525)$ are consistent with the previously known values [20–24].

The angular dependences of the differential cross section in the 2.4–3.3 GeV region are compared with $\sim 1/\sin^4\theta^*$ dependence, as found in the $\pi^0\pi^0$ process [11] and predicted by the handbag model [15,16] for $W > 3.1$ GeV. However, in the $\eta\eta$ process, a $1/\sin^4\theta^*$ dependence is not found in the data for the energy region where the measurement is performed.

The slope parameter n for the cross section, $\sigma(W) \sim W^{-n}$, in a similar W region is close to that measured in the $\pi^0\pi^0$ process [11].

The measured cross section ratio $\sigma(\eta\eta)/\sigma(\pi^0\pi^0) = 0.37 \pm 0.02 \pm 0.03$ (for $|\cos\theta^*| < 0.8$) is compared with the prediction of pQCD [14] with a pseudoscalar meson mixing angle $\theta_P = -18^\circ$. We find that the assumption for the squared form-factor ratio, $R_f = (f_\eta/f_{\pi^0})^2 = 1$, which is in good agreement with the ratio $\sigma(\eta\pi^0)/\sigma(\pi^0\pi^0)$ [12], cannot reproduce well the $\eta\eta$ measurement. Our result agrees rather well with the recent handbag model prediction [16].

Charmonium contributions in the $\eta\eta$ process are confirmed for the first time. Our measurements are consistent with the known partial decay widths of χ_{c0} and χ_{c2} to $\gamma\gamma$ [20] and $\eta\eta$ [28,29] final states.

ACKNOWLEDGMENTS

We thank the KEKB group for the excellent operation of the accelerator, the KEK cryogenics group for the efficient operation of the solenoid, and the KEK computer group and the National Institute of Informatics for valuable computing and SINET3 network support. We acknowledge support from the Ministry of Education, Culture, Sports, Science, and Technology (MEXT) of Japan, the Japan Society for the Promotion of Science (JSPS), and the Tau-Lepton Physics Research Center of Nagoya University; the Australian Research Council and the Australian Department of Industry, Innovation, Science and Research; the National Natural Science Foundation of China under Contracts No. 10575109, No. 10775142, No. 10875115, and No. 10825524; the Ministry of Education, Youth and Sports of the Czech Republic under Contract No. LA10033; the Department of Science and Technology of India; the BK21 and WCU program of the Ministry Education Science and Technology, National Research Foundation of Korea, and NSDC of the Korea Institute of Science and Technology Information; the Polish Ministry of Science and Higher Education; the Ministry of Education and Science of the Russian Federation and the Russian Federal Agency for Atomic Energy; the Slovenian Research Agency; the Swiss National Science Foundation; the National Science Council and the Ministry of Education of Taiwan; and the U.S. Department of Energy. This work is supported by a Grant-in-Aid from MEXT for Science Research in a Priority Area (“New Development of Flavor Physics”) and from JSPS for Creative Scientific Research (“Evolution of Tau-lepton Physics”).

- [1] T. Mori *et al.* (Belle Collaboration), *Phys. Rev. D* **75**, 051101(R) (2007).
 [2] T. Mori *et al.* (Belle Collaboration), *J. Phys. Soc. Jpn.* **76**, 074102 (2007).

- [3] H. Nakazawa *et al.* (Belle Collaboration), *Phys. Lett. B* **615**, 39 (2005).
 [4] K. Abe *et al.* (Belle Collaboration), *Eur. Phys. J. C* **32**, 323 (2004).

- [5] W. T. Chen *et al.* (Belle Collaboration), *Phys. Lett. B* **651**, 15 (2007).
- [6] C. C. Kuo *et al.* (Belle Collaboration), *Phys. Lett. B* **621**, 41 (2005).
- [7] S. Uehara *et al.* (Belle Collaboration), *Phys. Rev. Lett.* **96**, 082003 (2006).
- [8] S. Uehara *et al.* (Belle Collaboration), *Phys. Rev. Lett.* **104**, 092001 (2010).
- [9] C. P. Shen *et al.* (Belle Collaboration), *Phys. Rev. Lett.* **104**, 112004 (2010).
- [10] S. Uehara *et al.* (Belle Collaboration), *Phys. Rev. D* **78**, 052004 (2008).
- [11] S. Uehara *et al.* (Belle Collaboration), *Phys. Rev. D* **79**, 052009 (2009).
- [12] S. Uehara *et al.* (Belle Collaboration), *Phys. Rev. D* **80**, 032001 (2009).
- [13] See, e.g., the compilation in <http://durpdg.dur.ac.uk/spires/hepdata/online/2gamma/2gammahome.html>.
- [14] S. J. Brodsky and G. P. Lepage, *Phys. Rev. D* **24**, 1808 (1981).
- [15] M. Diehl, P. Kroll, and C. Vogt, *Phys. Lett. B* **532**, 99 (2002).
- [16] M. Diehl and P. Kroll, *Phys. Lett. B* **683**, 165 (2010).
- [17] A. Abashian *et al.* (Belle Collaboration), *Nucl. Instrum. Methods Phys. Res., Sect. A* **479**, 117 (2002).
- [18] S. Kurokawa and E. Kikutani, *Nucl. Instrum. Methods Phys. Res., Sect. A* **499**, 1 (2003), and other papers included in this volume.
- [19] S. Uehara, KEK Report No. 96-11, 1996.
- [20] C. Amsler *et al.* (Particle Data Group), *Phys. Lett. B* **667**, 1 (2008), and 2009 partial update for the 2010 edition.
- [21] F. Binon *et al.*, *Yad. Fiz.* **68**, 998 (2005) [*Phys. At. Nucl.* **68**, 960 (2005)].
- [22] D. Barberis *et al.* (WA102 Collaboration), *Phys. Lett. B* **479**, 59 (2000).
- [23] F. Binon *et al.*, *Yad. Fiz.* **70**, 1758 (2007) [*Phys. At. Nucl.* **70**, 1713 (2007)].
- [24] R. S. Longacre *et al.*, *Phys. Lett. B* **177**, 223 (1986).
- [25] J. M. Blatt and V. F. Weisskopf, *Theoretical Nuclear Physics* (Wiley, New York, 1952), pp. 359–365 and 386–389.
- [26] G. Grayer *et al.*, *Nucl. Phys.* **B75**, 189 (1974); A. Garmash *et al.* (Belle Collaboration), *Phys. Rev. D* **71**, 092003 (2005); B. Aubert *et al.* (BABAR Collaboration), *Phys. Rev. D* **72**, 052002 (2005).
- [27] V. L. Chernyak, arXiv:0912.0623.
- [28] D. M. Asner *et al.* (CLEO Collaboration), *Phys. Rev. D* **79**, 072007 (2009).
- [29] M. Ablikim *et al.* (BES Collaboration), *Phys. Rev. D* **81**, 052005 (2010).